Helwan University
Faculty of Science

GEM Performance Studies in CMS Experiment with Four Muons Final State

Thesis Submitted
In
Partial Fulfillment for the requirement of
Master degree of Science (Nuclear Physics)

To
Physics department, Faculty of Science
Helwan University, Cairo, Egypt

By
Waleed Ahmed Mohammed Esmail
B.Sc. Physics, 2009

2016

GEM Performance Studies in CMS Experiment with Four Muons Final State

Thesis Submitted
In
Partial Fulfillment for the requirement of
Master degree of Science (Nuclear Physics)

To
Physics department, Faculty of Science
Helwan University, Cairo, Egypt

By
Waleed Ahmed Mohammed Esmail
B.Sc. Physics, 2009

Supervisors:

1. Prof. Dr. Mohamed Nabil Yasein.
Physics Department, Faculty of Science, Helwan University.

2. Dr. Ahmed Ali Abdelalim.
Physics Department, Faculty of Science, Helwan University.

3. Dr. Yasser Mohamed Assran.
Math and Science Department, Faculty of Pet. and Min. Engineering, Suez University.

Dedicated To the soul of my Father ...

Acknowledgements

Firstly, I would like to express my sincere gratitude to my advisor Prof. Mohammed N.Yaseen, Professor, in Physics department at Helwan University for his continuous support of my Master study and related research, for his patience, motivation, and immense knowledge. His guidance helped me in all the time of research and writing of this thesis. I could not have imagined having a better advisor and mentor.

I want to express my grateful to my advisor Dr. Ahmed Ali Abdelalim, Lecture in Physics Department of Helwan University for his continual patience, outstanding guidance, invaluable discussions, support in various ways throughout my work, sharing expertise, support he has given me throughout this work and giving me the chance to run this work.

Special thanks to my advisor Dr. Yasser Assran, Physics Department of Suez Canal University, for his continual patience and helping me in the GEM performance part of my thesis.

My sincere thanks also goes to Prof. Amr Mohammed, Professor of Physics, Center for Fundamental Physics, Zewail City for Science and Technology, for his insightful comments and encouragement, but also for the hard question which incented me to widen my research from various perspectives.

Special thanks to Dr. Mohamed Attia, Physics Department of Fayoum University, for helping me in the first time in dealing with CMS software.

Also I wish to thank Prof. Amin Fahiem, Professor, at Physics department of Helwan University for his advice, help and support. And I take this opportunity to express gratitude to all the staff of the physics department at Helwan University for kind collaboration, help and support.

Special thank to my friends for their kind help and support.

Many thanks to my dear wife, for her support and endless patience, I am indebted to you for your unconditional love and care, and helping me in writing my master thesis.

Last but not the least, I would like to thank my family, for supporting me spiritually throughout writing this thesis and my life in general.

Waleed,

Abstract

The standard model (SM) of particle physics, although it is a very successful theory and compatible with all experimental results, it has a number of shortcomings, in particular it provides no answer for the three generations of fermions. Compositeness models try to solve this problem by postulating that quarks and leptons might be composite objects of fundamental particles. Due to their substructure, these models predict the existence of excited states of SM particles, in particular excited quarks q^* and excited leptons l^*.

In the first part of the thesis we present a phenomenological study of excited muons μ^* at center of mass energy $\sqrt{s} = 14$ TeV and integrated luminosity of $300 fb^{-1}$ respectively. These excited muons are produced via contact interactions at an energy scale Λ either singly in conjunction with a SM particle or in pairs. The considered channel here is the single production, in particular the decay channel $pp \to \mu\mu^* \to \mu\mu Z$, with the Z gauge boson decaying into two muons. So there will be 4μ final state, and it will be considered as a signature in the detector.
Although this branching ration is small; it is considered a clean channel. The main irreducible background is $pp \to ZZ \to 4\mu$. It is irreducible and overwhelming contributes about 90% of the total background expectations. The compositeness scale Λ, and the mass of the excited muon are free parameters in the theory. The mass range considered is between ($0.5 \sim 5$ TeV) with a step of 0.5TeV, and a compositeness scale $\Lambda = 10$ TeV.

Signal samples are generated using Pythia 8.2 Monte Carlo event generator at Leading Order (LO) accuracy using CTEQ6L1 parton distribution function (PDF). The signal events are then passed to Delphes fast simulation tool to simulate the CMS detector response and reconstruct the final state particles. Some SM processes give the same final state as our signal, and is considered as a background.

Background events is generated using Madgraph event generator interfaced with pythia for haronization and parton showering, and then passed to Delphes for detector simulation.

In the second part of the thesis, we provide a GEM performance study using the four muon channel of excited muons. **G**as **E**lectron **M**ultiplier is gaseous detector that would be introduced in high eta end-cap region of CMS detector at 2019 for tracking and triggering of muons as it can effectively differentiate effectively between low p_T and high p_T muons. The installation of GEM will restore robustness and redundancy thereby affording fully efficient and clean reconstruction of muons by improving muon momentum resolution and providing a highly efficient trigger and reconstruction capability.

List of Figures

List of Tables

Contents

Chapter 1

The Standard Model and Beyond

1.1 Introduction

Particle physics tries to answer the ancient question "What is the world made of?!". The ancient Greeks were the first to answer this question by proposing that matter is composed of tiny fundamental particles or building blocks they called atoms.

It was only in more recent times that individual elements or atoms were discovered. In 1879 J.J Thomson discovered the electron with his famous experiment on Cathode Ray Tube, soon afterwards Sir Rutherford through his most famous experiment theorized the atoms have their charge concentrated in a very small nucleus (10^{-5} times the size of the atom) and containing almost all the mass of the atom, subsequently the hydrogen nucleus was called the proton, but it was not until 1932 with Chadwick's discovery of the neutron the structure of the atom become clear. These three particles accounted for the structure of matter. But with the discovery of positrons, muons, pions, strange particles, neutrinos and a plethora of other particles, a whole new world was uncovered.

Due to this plethora of elementary particles Murray Gell-Mann in 1961 introduced the so called Eight-Fold Way which is considered as a periodic table of elementary particles. Eight-Fold Way arranged particles in various symmetrical geometrical patterns according to their quantum numbers, this scheme was very successful and led to the prediction of a particle called Ω^-. In 1964 the Quark Model was introduced by Gell-Mann and Zweig to explain the structure of the Eight-Fold Way. They proposed that all hadrons are composite particles made of particles called quarks. The Quark Model gained acceptance, and by 1978 a well-tested theory called the Standard Model of particle physics had emerged which accommodate all experimental observations in the simplest manner.

1.2 The Standard Model

The **S**tandard **M**odel (SM) of particle physics [1, 2] postulates that the universe we live in consists of three families of fermions classed into leptons and quarks. These classification is according to the way quarks and leptons interact, and for each fermion there exist an anti-fermion of the same mass and quantum numbers except of an opposite electric charge.

Up until the moment of writing this thesis, there are four known fundamental forces of nature which are gravity, weak force, electromagnetic force, and strong force. All forces or some of them exist between the fundamental particles of the SM and all of them are non contact forces, which means that there exist a force carrier (mediator) between particles. However at accelerator energies, gravity is a weak force relative to the others, consequently the SM explains only the three other forces.

The forces between the fermions are mediated by particles known as gauge bosons. The force is visualized as being due to the exchange of field quanta which arise in the framework of **Q**uantum **F**ield **T**heory (QFT) [3].

The SM combines **Q**uantum **C**hromo-**D**ynamics (QCD) and **E**lectro-**E**eak (EW) theory to describe particles and their interactions in the framework of QFT.

1.2.1 Fermions

Fermions are half-integer spin particles which obey Fermi-Dirac statistics and Pauli Exclusion Principle, they are further divided into Leptons and Quarks. Both quarks and leptons are organized in three generation families.

- Leptons: The leptons are; electron (e), muon (μ), tau (τ), neutrino electron (ν_e), neutrino muon (ν_μ) neutrino tau (ν_τ) and their corresponding anti-leptons. The electron, muon, and tau interact via electromagnetic and weak force, while neutrinos interact only via weak force.

- Quarks: The quarks are: up (u), down (d), strange (s), charm (c), bottom (b), top (t), and their corresponding anti-quarks. The quarks carry a fractional charge, and interact via strong force as well as electromagnetic and weak forces.

The strong force binds quarks together to form mesons (quark-antiquark pair), baryons (three quarks bound state), and anti-baryons (three anti-quarks bound state). Because quarks obey Pauli exclusion principle they cannot form a baryon unless they assigned a "color charge", it was formulated that each quark comes in three colors, red, green, and blue. These colors have nothing to do with actual color, they are just labels to distinguish among different quarks.

1.2.2 Interactions and their Mediators

Interactions are the way that particles influence each other, all particles and anti-particles in the SM interact via three of the fundamental forces, electromagnetic, weak, and strong interactions.

Each Force in the SM is described by exchange of a field quanta called gauge boson. These bosons are spin-1 particles, and obey Bose-Einstein statistics. The different interactions that the SM describe are summarized below:

- Electromagnetic interaction: The electromagnetic interaction occurs between particles that carry electric charge and it is a long range force. The electromagnetic interaction framework is called **Q**uantum **E**lectrodynamics (QED). The field quanta of QED is the photon (γ). Thus photons are the mediator of electromagnetic interaction. Now we know that QED is a U(1) Abelian gauge group [4, 5]; that is it obeys the symmetry of U(1) group.

- Weak interaction: The weak interaction acts between quarks and leptons and it is a short range force (10^{-18} m). Weak interaction is classified into charged or neutral interactions depending on whether the particle participating in a weak interaction suffers a change of electric charge or not. The weak force is mediated by the massive ($W\pm$) and (Z_0) gauge bosons. It is best understood in terms of EW theory [6].

- Strong interaction: Color charges gives rise to the strong interaction which binds quarks together to form hadrons (baryons and mesons) as well as binding protons and neutrons to form nuclei. The gauge bosons that mediate the strong force are the gluons (g), gluons are mass-less and so the strong force is a long range force. There are eight gluons which carry color charge, and consequently gluons have self interaction vertices according to the QFT. QCD is the gauge theory associated with strong interaction, which described by the group SU(3). In QCD, no individual quark can be detected, this feature can be explained by color confinement hypothesis which states that no object with non-zero color charge can propagate as a free particle [7].

The relative strengths of the forces associated with the different gauge bosons are indicated in table [1.1]. It should be noted that these numbers are indicative and the strengths of the forces may depend on the distance and energy scale being considered.

Force	Strenght	Gauge Boson
Strong	~ 1	Gluons
Electromagnetic	$\sim 10^{-3}$	Photons
Weak	$\sim 10^{-8}$	$W\pm$ and Z_0

Table 1.1: The relative strengths of fundamental forces of the SM at distance of 10^{-15} m.

1.2.3 Higgs Boson

The final element of the SM is the Higgs boson, which was discovered recently in July 2012 by the ATLAS and CMS collaborations independently at the Large Hadron Collider (refer to chapter 2). The Higgs boson plays a special role in the SM; it provides the mechanism by which all other particles acquire mass.

The mechanism of which particle acquire mass in a process known as spontaneous **E**lectro-**W**eak **S**ymmetry **B**reaking (EWSB) of Higgs mechanism, the idea is to suppose that the vacuum contains a background scalar field known as the Higgs field [8], this field has a nonvanishing vacuum expectation vale (VEV) for the ground state so that it is no longer an exact symmetry of the Lagrangian. The symmetry is not destroyed but it is merely rendered hidden. The result is that the $W\pm$ and Z_0 quanta, when propagating through the Higgs field acquire mass.

Fundamental particles, and force mediators and their corresponding properties are shown in figure [1.1].

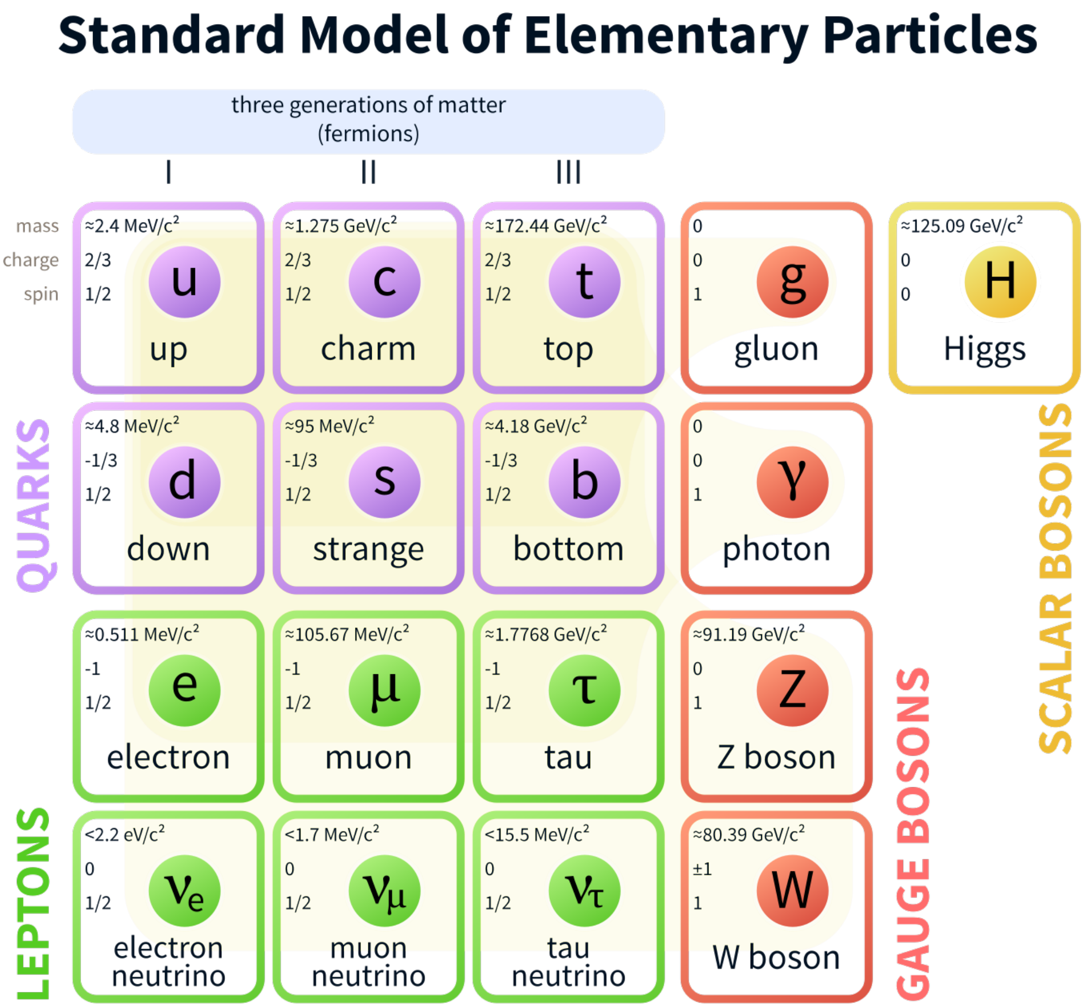

Figure 1.1: Fermions and gauge bosons of the Standard Model of Particle Physics.

1.3 Motivations to go Beyond The Standard Model

The Standard Model has been tested for decades and has proven to be extremely successful. Although, it is rightly believed that it is not the complete or the final answer. There are fundamental physical phenomena in nature that the Standard Model does not adequately explain, these are summarized below:

- **Gravity**: the SM does not account for the gravitational force, moreover the SM is not compatible with the most successful theory of gravity to date, the *General Theory of Relativity.*
- **Neutrino masses**: according to the SM, neutrino are mass-less particles. However experiments show that a neutrino created with specific flavor can be measured to have a different flavor. These neutrino oscillation experiments is not possible if the neutrino have zero mass.
- **Dark matter and Dark energy**: some cosmological observations tell us the SM explains about 5% of the matter and energy present in the universe, the rest is the so called Dark matter 26%, and Dark energy 69%. The SM does not support any fundamental particles that are good dark matter candidate, yet the SM does not explain dark energy [9].
- **Matter anti-Matter asymmetry**: The atoms in our local region of the Universe are formed from matter particles, rather than their equivalent anti-matter particles. The predominance of matter is believed to have arisen in the early universe. The predominance of matter over anti-matter can be attributed to violation of the CP symmetry. Yet, no mechanism sufficient to explain this asymmetry exists in the SM and CP-violation incorporated into the CKM matrix [10] is indeed not enough.
- **Free parameters**: the SM contains 19 free parameter that must be determined by experiment, and offers no explanation for many of the puzzling aspects such as the origin of the free parameters.
- **Hierarchy problem**: one of the fundamental questions of particle physics is why there are so many orders of magnitude between the Planck scale (10^{-35} m) and the weak scale (10^{-8} m) without any intermediate physics.
- **Three generations of matter**: the SM is unable to explain why there are three generations of quarks and leptons, why there is a mass spectrum of generations.

1.4 Compositeness of Fermions

Compositeness models [11, 12, 13] tries to solve some of the shortcomings of the SM. It assumes that particles of the SM are not anymore fundamental, but composed of more fundamental particles called *preons* which interact via a new strong gauge interaction.

Different reasons come to mind to motivate this idea, first of all the proliferation of particles, second the large numbers of free parameters of the SM, and the need to compute the parameters of the model from some deeper theory, third the gap between the weak and gravity scales (10^{-8} and 10^{-35} m respectively), and finally may be the mankind's curiosity to know the most fundamental building blocks of our universe.

Below a certain characteristic scale called *Compositeness Scale* Λ, the gauge interaction becomes strong and binds the preons together to form quarks, leptons and heavy bosons. The signature for this compositeness could be a significant deviation in the measured cross section at large center of mass energy compared to the predictions of the Standard Model.

If quarks and leptons have substructure, we expect them to exhibit excited states just like atoms; that is because atoms have internal structure if we give it some energy it will be in an excited state, so also for SM particles. From now on we will focus on the excited leptons.

1.4.1 Production of excited leptons via contact interactions

If the scale of compositeness is low compared to the center of mass energy available ($\Lambda < \hat{s}$), where $\hat{s}$ where is the center of mass energy for partons (refer to chapter 3), narrow resonances of excited particles can be produced on shell. On the other hand if ($\Lambda > \hat{s}$), compositeness production will manifest as a four fermion **C**ontact **I**nteraction (CI) [14]. This production can be described by an effective Lagrangian:

$$\mathcal{L}_{CI} = \frac{2\pi}{\Lambda^2} j^\mu j_\mu \tag{1.1}$$

where j^μ is the fermion current:

$$j^\mu = \bar{f}_L \gamma^\mu f_L + \bar{f}^*_L \gamma^\mu f^*_L + \bar{f}^*_L \gamma^\mu f_L + (L \to R) + h.c \tag{1.2}$$

where the ground state is f and the excited states is f^*, *"h.c."* stands for Hermitian conjugate, and the subscripts L refers to left-handed fermions, where right handed fermions are set to zero for simplicity. Excited fermions can be produced either by single production $qq \rightarrow \ell\ell^*$,double production $qq \rightarrow \ell^*\ell^*$ as shown in figure [1.2].

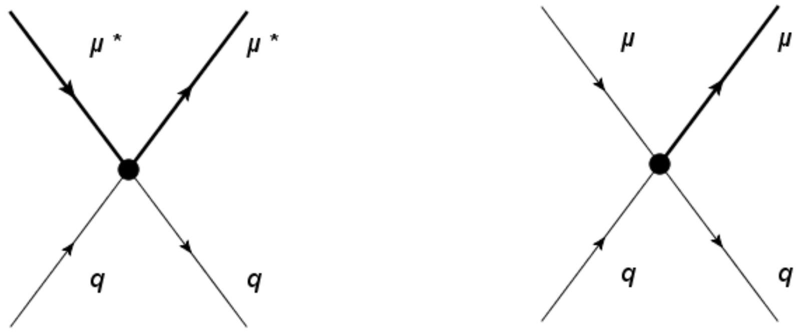

Figure 1.2: (Right) single production of μ^*, (Left) double production of μ^*

Since the pair production requires larger center of energy than the single production, it is kinematically less favored. figure [1.3] shows the cross section of single and double production of excited leptons.

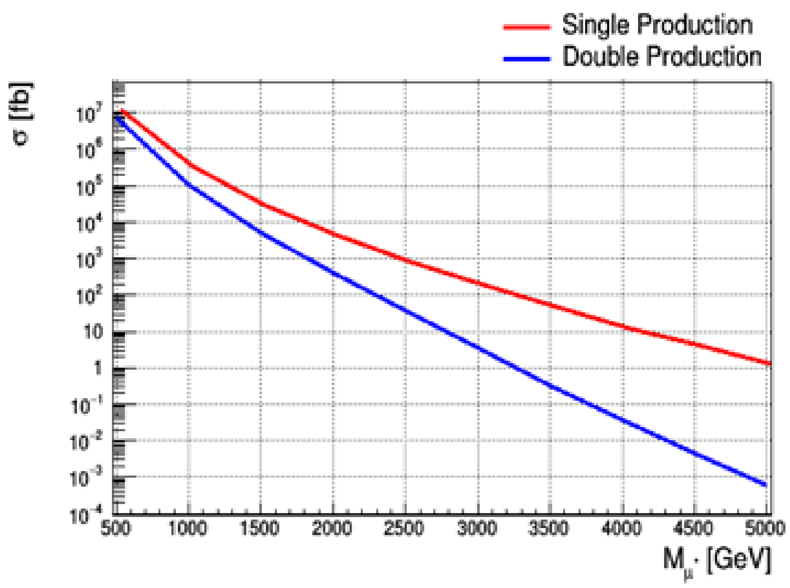

Figure 1.3: Cross section for single and double production of excited muons μ^* through contact interactions at LHC ($\sqrt{s} = 14$TeV, and, $\Lambda = m^*$), generation is done via Pythia8.

The partonic cross section, based on the effective Lagrangian of equation [1.1] with left-handed currents, are:

$$\hat{\sigma}(q\bar{q} \to \ell\bar{\ell}^*, \bar{\ell}^*\ell) = \frac{\pi}{6\hat{s}}(\frac{\hat{s}}{\Lambda^2})^2(1+\frac{\nu}{3})(1-\frac{m^{*2}}{\hat{s}})(1+\frac{m^{*2}}{\hat{s}}) \tag{1.3}$$

and,

$$\hat{\sigma}(q\bar{q} \to \bar{\ell}^*\bar{\ell}^*) = \frac{\pi\bar{\nu}}{12\hat{s}}(\frac{\hat{s}}{\Lambda^2})^2(1+\frac{\bar{\nu}^2}{3}) \tag{1.4}$$

where,

$$\nu = \frac{\bar{s}-m^{*2}}{\bar{s}+m^{*2}}, \qquad \bar{\nu} = 1-4\frac{m^{*2}}{\bar{s}}$$

Besides CI production, excited leptons can be also produced via gauge interactions (Lagrangian is described in the next subsection), however those processes contribute to less than 1% (depending on the excited lepton mass) compared to its production via CI [15].

1.4.2 Decay of excited leptons

Gauge-mediated transitions between SM and excited fermions are described by an effective Lagrangian [14]:

$$\mathcal{L}_{GM} = \frac{1}{2\Lambda}\bar{f}^*_R\sigma^{\mu\nu}\Big[g_s f_s G^a_{\mu\nu}\frac{\Lambda^a}{2} + gfW_{\mu\nu}\frac{\tau}{2} + g'f'B_{\mu\nu}\frac{Y}{2}\Big]f_L + h.c. \tag{1.5}$$

where $\sigma_{\mu\nu}$ is the covariant bilinear tensor, f, f^* are the lepton and excited lepton fields, $G^a_{\mu\nu}$, $W_{\mu\nu}$, and $B_{\mu\nu}$ are strength tensors of the gluon, $SU(2)_L$ and $U(1)_Y$ gauge fields with the group generators Λ^a (Gell-Mann matrices), τ (Pauli matrices), and Y (weak hypercharge) respectively; the factors f_s, f, and f' are form factors which determined by the composite dynamics. Naively one would except all of them to be of order 1, and g_s, g, g' are the corresponding coupling constants.

Here we assume that excited leptons have a mass larger than the W$\pm$ and Z_0 boson masses and the main decay mode via gauge interaction will be two-body decays shown in figure [1.4] (left) alongside with the CI decay process.

The partial decay widths for the gauge mediated interactions are given by [14]:

$$\Gamma_{GM}(\ell^* \to \ell\gamma) = \frac{\alpha}{4} f_\gamma^2 \frac{m_*^3}{\Lambda^2} \tag{1.6}$$

$$\Gamma_{GM}(\ell^* \to \ell V) = \frac{1}{8}\frac{g_V^2}{4\pi} f_V^2 \frac{m_*^3}{\Lambda^2}(1 - \frac{m_V^2}{m_*^2})^2(2 + \frac{m_V^2}{m_*^2}) \tag{1.7}$$

where α is the fine structure constant, V stands for W± or Z_0, and g_V s the coupling constant associated with the gauge boson V, f_V and f_γ are given by:

$$f_\gamma = f I_3^W + f' \frac{Y}{2}$$

$$f_W = \frac{f}{\sqrt{2}}$$

$$f_\gamma = f I_3^W cos^2\theta_w + f' \frac{Y}{2} sin^2\theta_w$$

where I_3^W, and Y are the third component of weak isospin and hypercharge of excited lepton respectively, and θ_w is the weak mixing angle.

The widths can however be significantly increased by decays which are mediated by contact interactions (three-body decay) from eqations [1.1], [1.2]:

$$\Gamma_{CI}(\ell^* \to \ell + \ell'\bar{\ell}') = \frac{m_*}{96\pi}(\frac{m_*}{\Lambda})^4 N_c' S' \tag{1.8}$$

where N_c'=3 or 1 is the number of colors of the light fermion f', and S' is an additional combinatorial factor:

$$\begin{array}{lll} S' = 1 & for & f \neq f' \\ S' = 4/3 & for & f = f' \quad and quarks, \\ S' = 2 & for & f = f' \quad and leptons. \end{array}$$

For this analysis we assume that $f = f'$=1 but the results can easily be reinterpreted for different values of these parameters, accounting for the change in branching ratio and intrinsic width.

Although the decay by CI dominates for large values of m_*/Λ, the decay via gauge interactions proportional to m_*^3/Λ^2 while decay via CI varies as m_*^5/Λ^4. Therefore, the relative importance of the decay mediated by contact interaction on the total decay width will be suppressed by the factor m_*^2/Λ^2. This behavior is clearly illustrated in figure [1.5] which shows the branching fraction of the decay of excited lepton via CI as well as that of gauge interaction decay.

Figure 1.4: Decay of excited lepton μ^* into a lepton μ and a pair of leptons via gauge interactions mediated by the vector boson (left), and via CI (right)

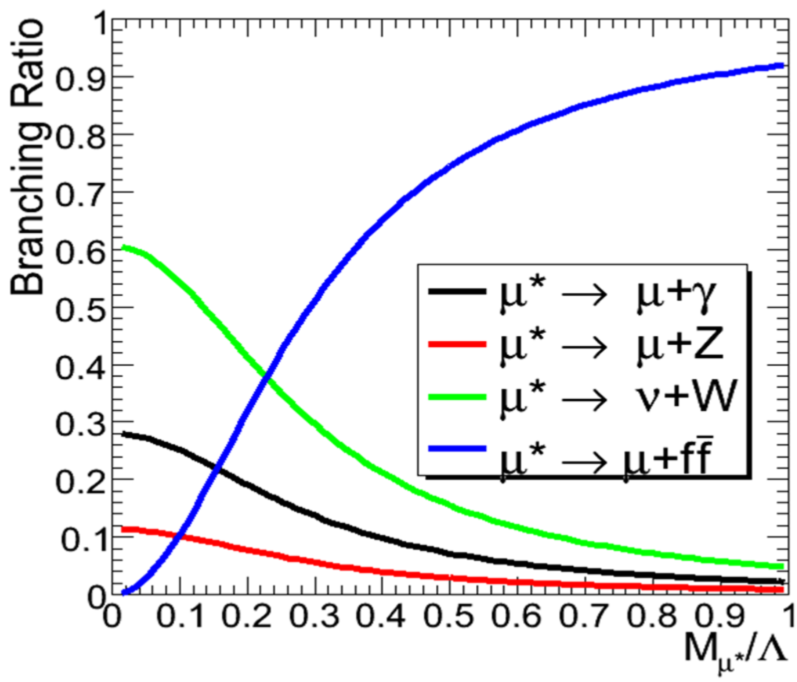

Figure 1.5: Branching fractions of the excited leptons as a function of $\frac{m_*}{\Lambda}$

1.5 Previous searches of compositeness

Up to date there is no experimental evidence of the compositeness of particles of the SM. Various experiments have tested many such models and has evaluated bounds on the parameters such as the compositeness scale Λ or the excited lepton mass m_*, different decay modes of the excited states probe different aspects of the effective theory that govern the low energy interaction.

The experimental previous results are listed below:

- **HERA**: The **H**adron **E**lectron **R**ing **A**ccelerator (HERA) at DESY, Hamburg operated during 1992-2007 using $e^{\pm}$p data at energy of 27.5 GeV and an integrated luminosity of $37pb^{-1}$ searched for excited fermions [16, 17]. By assuming that $f/\Lambda = 1/m_*$, excited fermion mass below 223, 114, and 188 GeV, for e^*, ν^*, q^* production , respectively, are excluded [18]. figure [1.6] shows exclusion limits on the search of excited electron.

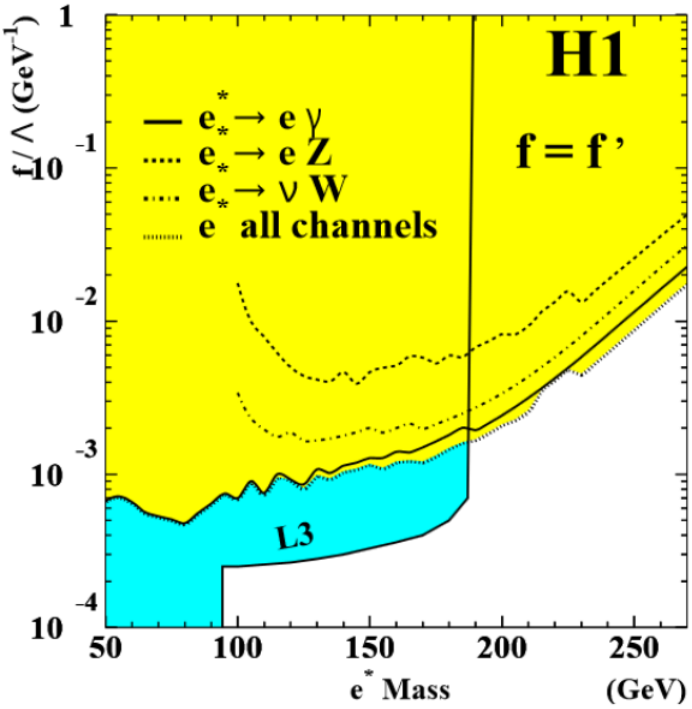

Figure 1.6: Limits on search for excited electron in H1 experiments at HERA

- **LEP**: the OPAL collaboration (at The **L**arge **E**lectron **P**ositron collider, CERN) at 2002 searched electromagnetic decays of e^*,

μ^*, and τ^* in the center of mass energy range of 183 -209 GeV. The final states, which have been studied, comprised of $\ell\ell\gamma$, and $\ell\ell\gamma\gamma$. The amount of data used was $680pb^{-1}$. From pair production searches the OPAL collaboration has put a lower bound of m^*_{ℓ}¿ 103.2 GeV with 95% confidence level. Figure [1.7] show the upper limits on the cross-section times branching ratio [19].

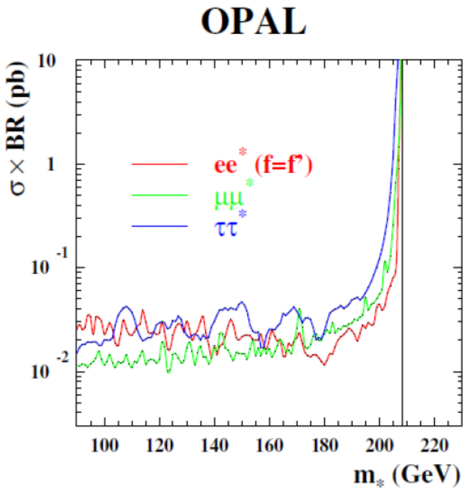

(a)

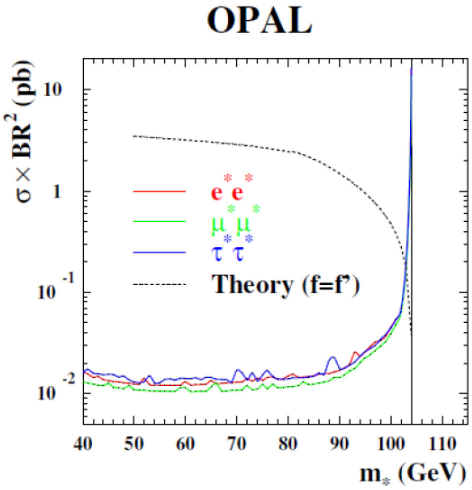

(b)

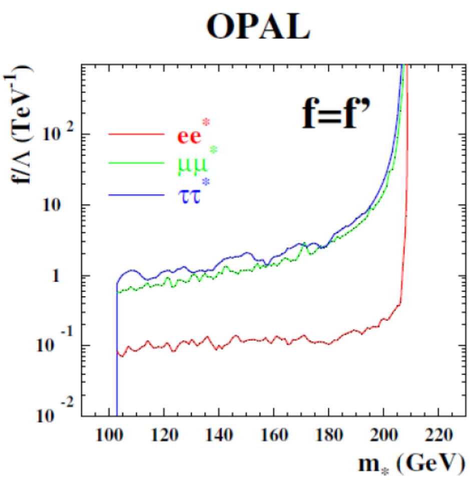

(c)

Figure 1.7: OPAL collaboration at LEP 95% CL upper limits on the cross-section at $\sqrt{s}$ = 208.3 GeV times the branching fraction for (a) single and (b) pair production of excited leptons as a function of mass. The 95% CL upper limits on the ratio of the excited lepton coupling constant to the compositeness scale, f/Λ as a function of the excited lepton mass assuming $f = f'$ are shown in (c).

- **TEVATRON**: the Tevatron at Fermi National Accelerator Laboratory (Fermilab) is an accelerator with center of mass energy of $\sqrt{s} = 1.96$ TeV. The CDF collaboration at Tevatron searched for single production of excited electron and subsequent radiative decay with an amount of data of $202pb^{-1}$. CDF set a lower limit on the excited electron mass that produced by CI (see figure [1.8]) [20].

Also D0 collaboration at Tevaron using data size of $1fb^{-1}$ searched for single production of excited by the process $e^* \to ee\gamma$. D0 data is interpreted in the context of CI production model and decay via GM model. A lower mass limit of the excited electron of 756 GeV for $\Lambda = 1$ TeV was set as illustrated in figure [1.9] [21].

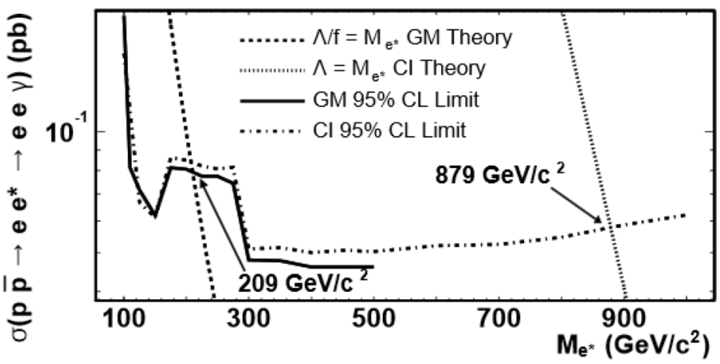

Figure 1.8: The experimental σ x BR limits for the CI and GM models compared to the theoretical predictions. The mass limits are indicated

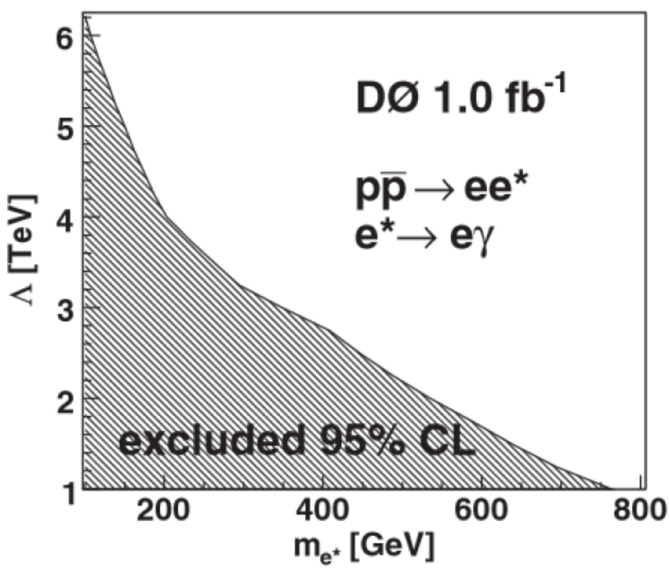

Figure 1.9: The region in the (Λ, m_e^*) plane excluded by D0 experiment.

- **CMS**: the Compact Muon Solenoid experiment at the Large Hadron Collider in 2012 (see chapter2) using a data sample of p-p collisions at a center-of-mass energy 7 TeV, and integrated luminosity of $5fb^{-1}$ searched for radiative decay of excited muons, and excited electrons [22], for the case of $\Lambda = m^*_\ell$, excited leptons of masses below 1.9 TeV are excluded as shown in figure [1.10].

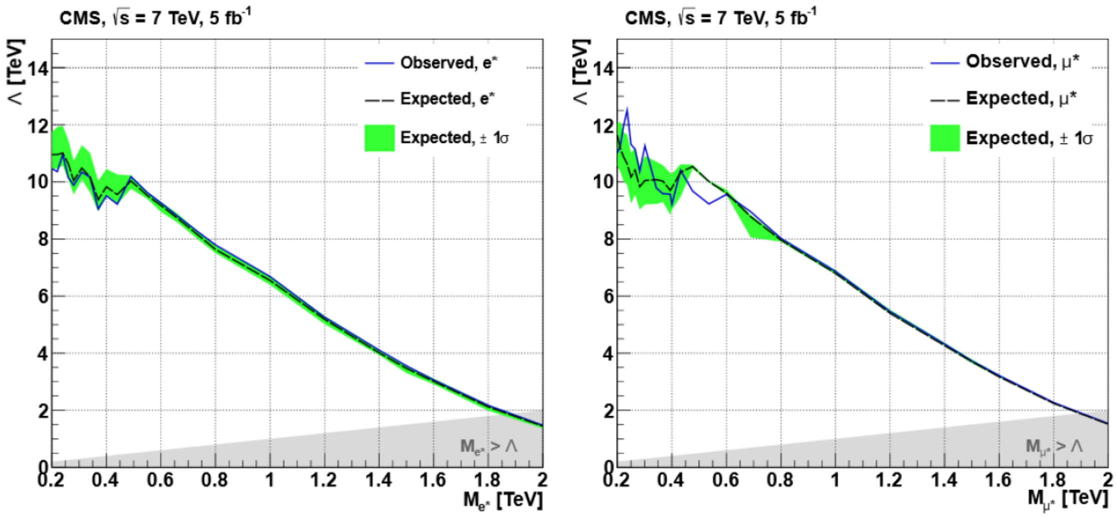

Figure 1.10: Expected and observed 95% CL lower limits on the Λ scale for the different excited electron (left) and muon (right) mass points, the excluded region is below the curve. The one standard deviation uncertainty band is shown in green. The grey area corresponds to the theoretically excluded region where $\Lambda < m^*_\ell$

- **ATLAS**: the A Toroidal LHC ApparatuS collaboration at LHC in 2013 (see chapter2) using a data sample of p-p collisions at a center-of-mass energy 8TeV, and integrated luminosity of $13fb^{-1}$ searched for radiative decay of excited muons, Limits on σxBR are converted into lower bounds on the compositeness scale [23]. In the special case where $\Lambda = m_{\ell}^{*}$, excited electron, and excited-muon masses below 2.2 TeV are excluded [1.11].

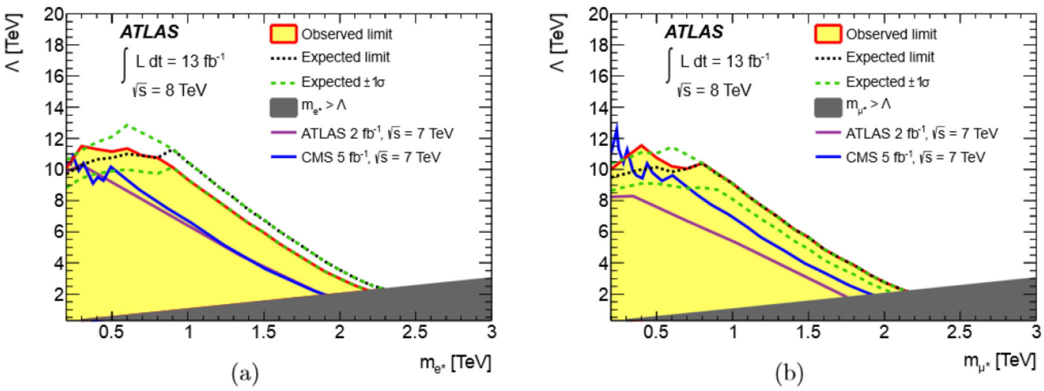

Figure 1.11: Exclusion limits in the compositeness scale Λ vs excitedlepton mass m_{ℓ}^{*} parameter space for the electron (a) and muon (b) channels. The filled area is excluded at 95% CL. No limits are set in the dark shaded region where the model is not $\Lambda < m_{\ell}^{*}$ applicable.

Chapter 2

Experimental Setup

2.1 The Large Hadron Collider

The **L**arge **H**adron **H**ollider (LHC) at the European Organization for Nuclear Research (known by its French acronym CERN) located on the Swiss-French border near Geneva, Switzerland is the world's most powerful proton-proton collider for the current generation of high-energy particle physics experiments [24]. The machine is located 100 meter underground in a ring of superconducting magnets and circumference of 27 kilometers. Two proton beams are accelerated in opposite directions around the ring, while LHC steers those protons to four interaction points. Each beam will have a 7 TeV thus giving total collision energy of 14 TeV in the center of mass frame.

Located at these interaction points are four major particle detector experiments, **A** **T**oroidal **L**HC **A**pparatu**S** [25] (ATLAS) and the **C**ompact **M**uon **S**olenoid [26] (CMS), A **L**arge **I**on **C**ollider **E**xperiment [27] (ALICE) and the **L**arge **H**adron **C**ollider **b**eauty [28] (LHCb) detector. These experiments collect and analyze data.

2.1.1 Principle of operation and future plans

Prior to being injected into the main accelerator, protons are obtained by ionizing gaseous hydrogen, and then accelerated in bunches to the linear accelerator (LINAC2), which is the first system of the accelerator, and speeds up the protons to energy of 50 MeV. From there they are injected into the **P**roton **S**ynchrotron **B**ooster (PSB) and boosted to energy of 1.4 GeV, and then they accelerate to 26 GeV in the **P**roton **S**ynchrotron (PS), the **S**uper **P**roton **S**ynchrotron (SPS) is used to further increase their energy to 450 GeV before they are at last injected into the LHC.

The particle beam is not a continuous flux but rather a series of bunches that are put into track and focused by a set of magnets. A schematic view of the CERN accelerator complex is shown in figure [2.1].

The collision rate is quantified in terms of the instantaneous luminosity (number of collisions per unit time per unit area), which depends on the configuration of the accelerator.

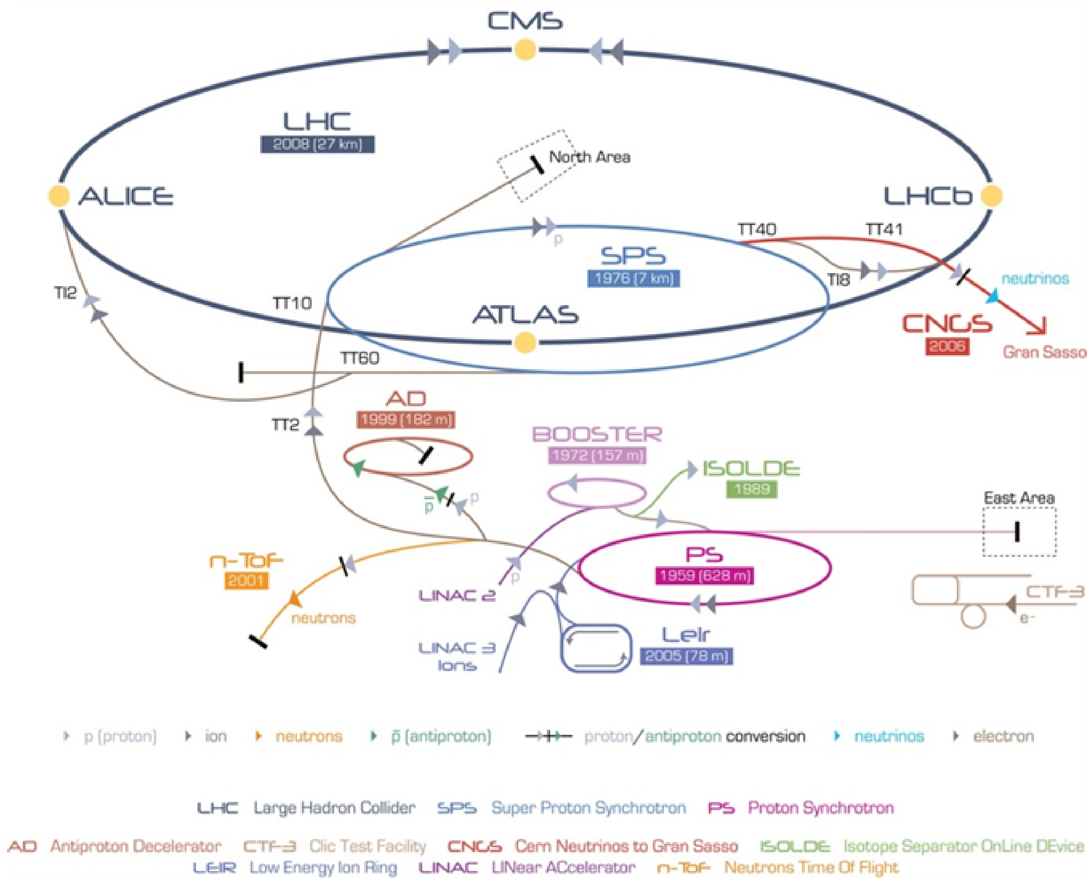

Figure 2.1: Schematic layout of the accelerator complex at CERN. The proton beams have a revolution frequency which is geometrically fixed by design, and are spaced by about 7 meters, which corresponds to 25 nanoseconds, and a frequency of 40 MHZ

The LHC's operation plan [29] is divided in two phases: phase 1 during which the machine will slowly reach its nominal capabilities, and phase 2 where the machine will run at even higher luminosity after undergoing a major upgrade. Table [2.1] shows the energy and luminosity of the operational periods of LHC after both maintenance **L**ong **S**hutdown 1 (LS1) and **L**ong **S**hutdown 2 (LS2).

Phase 2 will have a major upgrade of the LHC, which aims to increase the Luminosity and the machine will enter the new era of High- Luminosity LHC (HL-LHC).

Period	Energy [TeV]	Luminosity
2010-2012	7 -8	0.5x$10^{34} cm^{-2} s^{-1}$
2015-2018	13 - 14	1x$10^{34} cm^{-2} s^{-1}$
2021-2023	14	2x$10^{34} cm^{-2} s^{-1}$

Table 2.1: Energy and Luminosity of the LHC during the different periods of phase1.

2.2 Compact Muon Solenoid

The **C**ompact **M**uon **S**olenoid (CMS) detector [30] is one of the most complex detectors ever build. The design of the CMS is driven by the challenges of a physics experiment in the LHC environment. Many of the physics benchmark channels have a small cross section and the background from QCD jet production is overwhelmingly dominant. A high rejection power with an optimal efficiency for rare channels has to be achieved. The CMS, as its name suggests, is based in an intense solenoid magnetic field of 3.8 T, and an excellent muon spectrometer. A schematic diagram of the structure and different components of the CMS is show in figure [2.2].

The CMS detector is composed of the following main sub-detectors as one moves out from the center of the detector: the silicon tracker (TK), the electromagnetic calorimeter (ECAL), the hadronic calorimeter (HCAL), the solenoid magnet, and finally the muon system is outside the solenoid and inside the steel return yoke of the magnet. A transverse slice of CMS, showing the various sub-detectors is shown in figure [2.3].

Because it has a cylindrical shape CMS is divided into two regions: the barrel where the detectors are laid out cylindrically around the beam, and the endcaps where the detectors are placed perpendicularly to the beam.

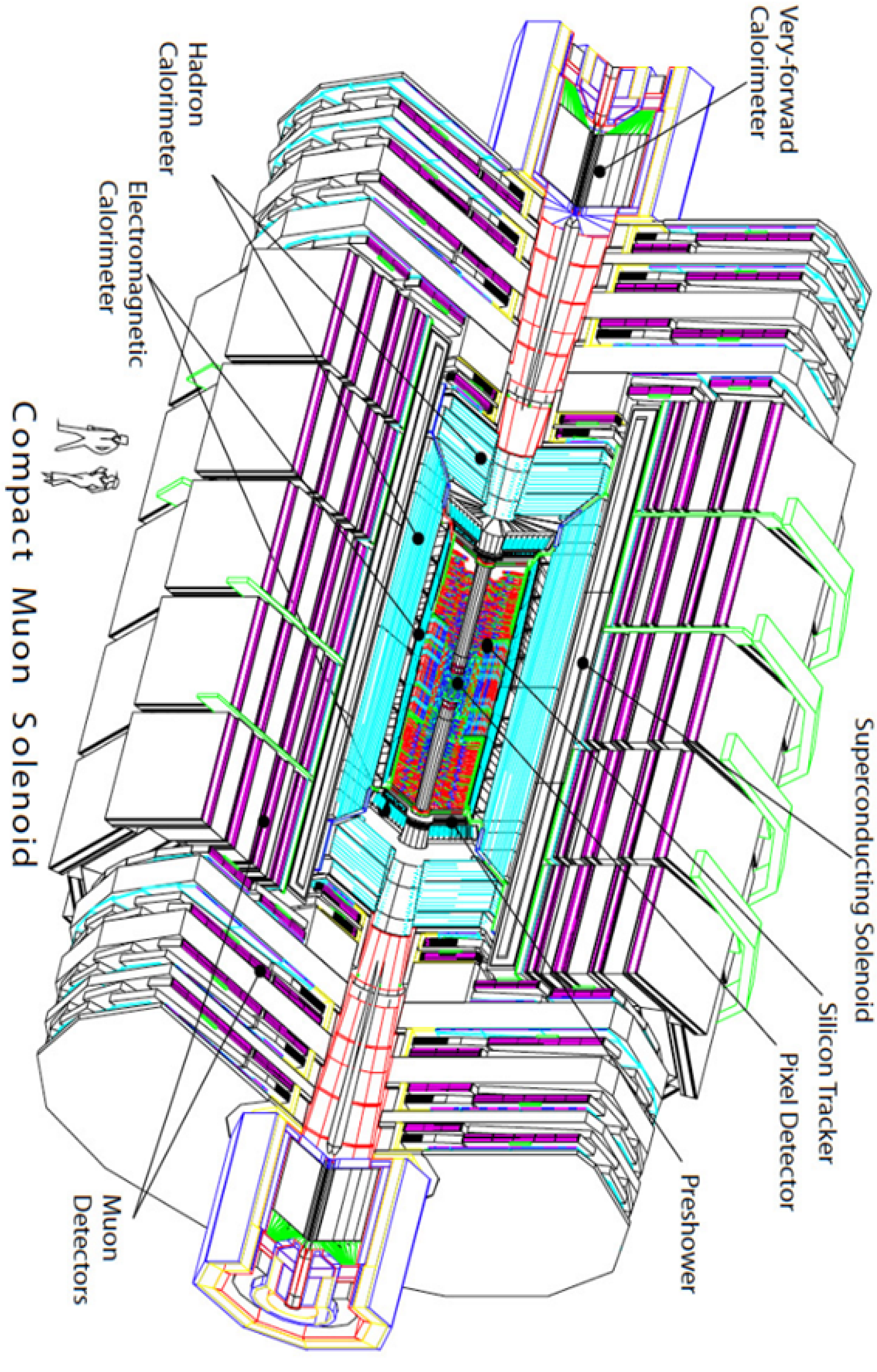

Figure 2.2: Representation of CMS and its different components.

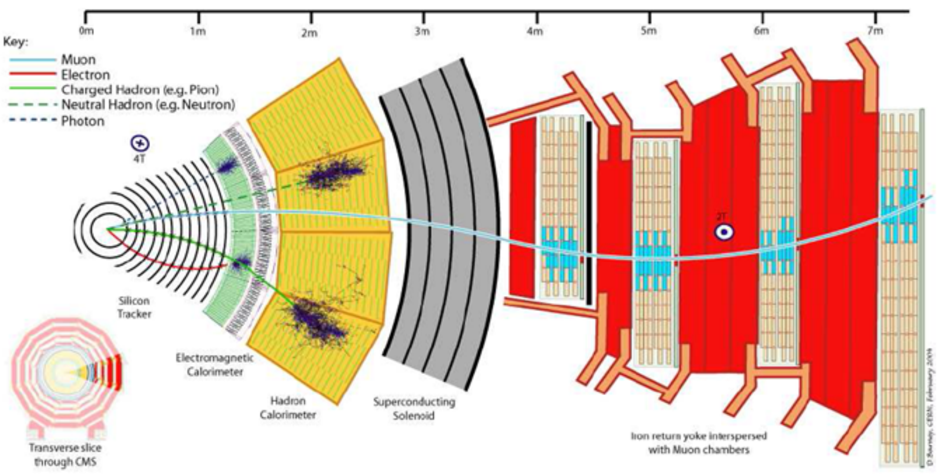

Figure 2.3: A transverse slice of the CMS sub-detectors with a representative detection of a particle in each sub-detector. Animated version for particles passing through each part can be found in [30]

2.2.1 Coordinate conventions of CMS

In CMS, the coordinate system has its origin centered at the nominal collision point. The y-axis points vertically upward and the x-axis points radially inward toward the center of the LHC tunnel. The z-axis points along the beam direction as show in figure [2.4].The azimuthal angle ϕ is measured from the x-axis in the $x-y$ plane, and the polar angle θ is measured from the z-axis, and expressed in terms of the Lorentz invariant quantity pseudo-rapidity:

$$\eta = -ln\Big[tan(\frac{\theta}{2})\Big] \tag{2.1}$$

The pseudo-rapidity η is preferred over the polar angle because the rate of production of relatively light particles such as pions and kaons at hadron colliders is approximately constant over a wide range of η. The momentum and energy measured transverse to the z-axis is denoted as p_T and E_T, respectively.

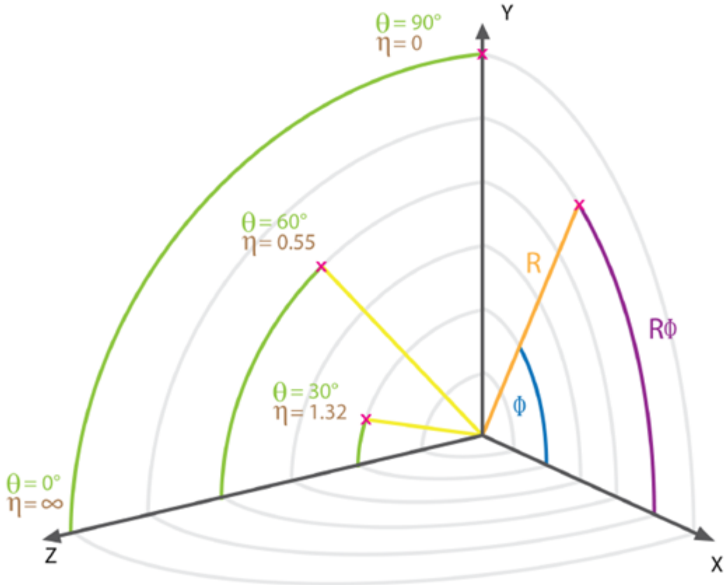

Figure 2.4: The pseudo-rapidity η, and azimuthal angle ϕ used to track particles inside CMS.

2.2.2 Tracking System

The innermost sub-detector that a particle coming from the interaction point traverses is the tracker [31]. Its purpose is to provide a precise and efficient measurement of the trajectories of charged particles as well as a precise reconstruction of interaction vertices. Knowledge of the primary interaction point is important, especially in the high instantaneous luminosity operations at the LHC, where multiple vertices are present for every collision because of multiple interactions in a phenomenon known as Pile-Up.

At the nominal design instantaneous luminosity of $10^{34} cm^{-2}s^{-1}$, there are on average about 1000 particles traversing the tracker per LHC bunch crossing, which requires a tracker detector with a high granularity and fast response. Also because of the higher particle rates at the center of the detector causes severe radiation damage to the tracker detector. Considering those requirements of granularity, fast speed and radiation hardness, CMS experiment built its tracker detector entirely based on the silicon detector technology.

The tracking system consists of two parts, the pixel detector (silicon pixels) and the inner tracker (silicon strips). Both are made of silicon. These detectors have an excellent spatial resolution ($\sim 25\mu$m).

A schematic cross section view of the tracking system is shown in figure [2.5].

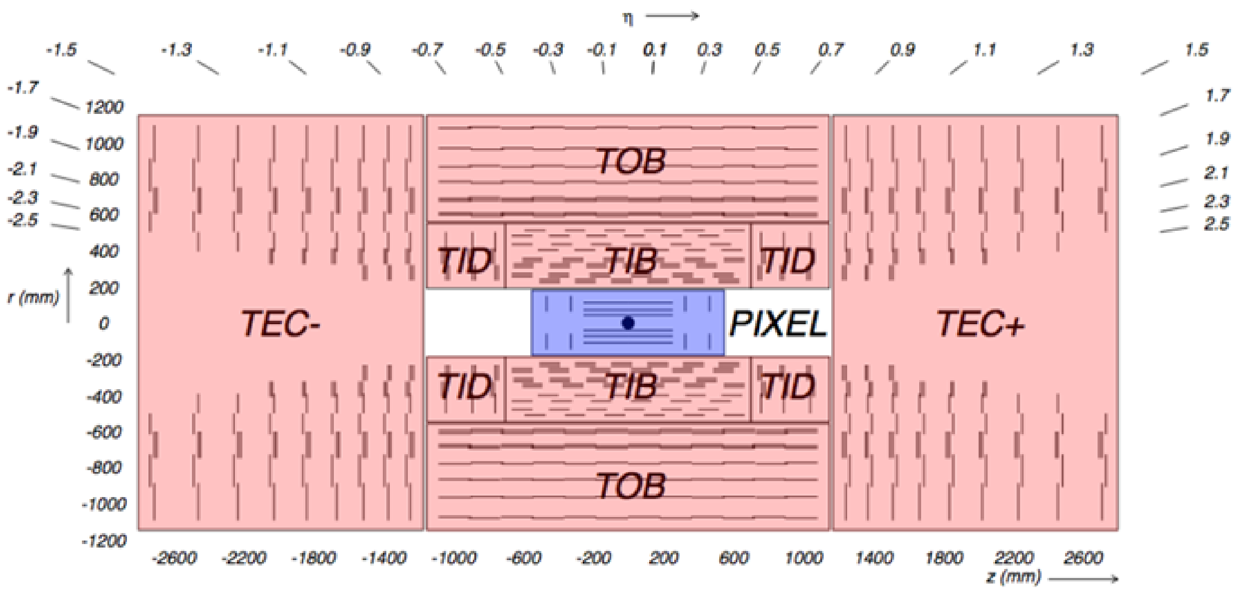

Figure 2.5: Schematic cross section of CMS tracker detectors. Each line represent a detector module or layer.

The silicon pixels are represented in blue, while the **T**racker **I**nner **B**arrel and **D**isks (TIB/TID), **T**racker **O**uter **B**arrel (TOB), and **T**racker **E**nd- **C**aps (TEC) are the different region of the silicon strip detector.

Semiconductor detectors are made out of series of p-n junctions. When a charged particle passes through the depletion region and losses energy, electrons switch from valence to conductive bands creating electrons/holes pairs. Under the action of the electric field, they migrate towards the n or p regions and form the signal on the readout electronics.

The barrel pixel detector consists of three layers, centered at approximately 4 cm, 7 cm and 11 cm radius, respectively. The forward pixel detector is made up of two pairs of layers at ±34 cm and ±46 cm from the nominal interaction point in beam axis direction. The geometrical arrangement is shown in figure [2.6].

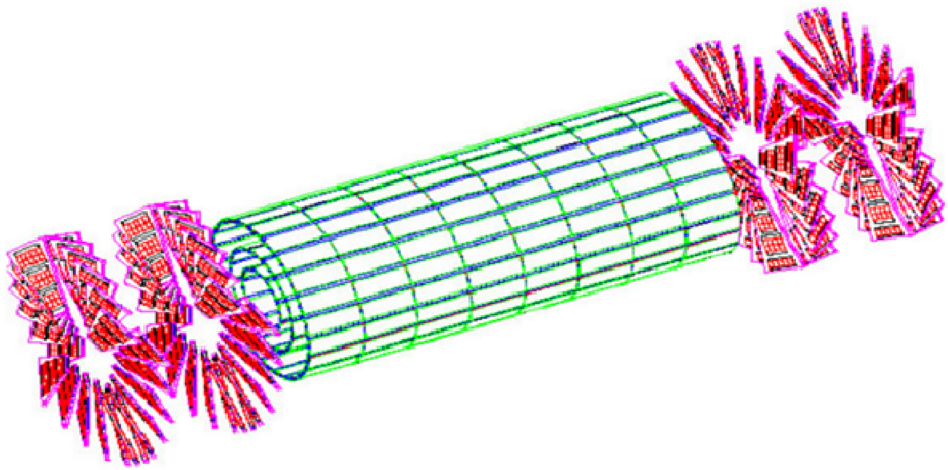

Figure 2.6: Schematic cross section of CMS tracker detectors. Each line represent a detector module or layer.

The inner tracker surrounding the pixel system is made of 15000 silicon micro-strip detector modules. Each module is made of a set of sensors, a mechanical support structure and a readout hybrid, which is bonded to the sensors. Geometrically the inner tracker modules are arranged in 10 concentric layers in the barrel and 12 disk-shaped layers in the forward regions.

Due to the harsh radiation environment and low-noise requirement the tracker has to be operated at a temperature of -10^{o}C.

2.2.3 The Electromagnetic Calorimeter

The **E**lectromagnetic **CAL**orimeter (ECAL) [32] is designed to measure with high accuracy the energies of electrons and photons. There are two main processes for allowing the detection of electrons and photons which are respectively *Bremsstrahlung* and *pair creation.* These two processes form what is called the *electromagnetic shower* that is formed when energetic photon or electron enters the ECAL material. Figure [2.7] shows a layout of the ECAL sub-detector.

The CMS ECAL consists of ECAL Barrel (EB), ECAL End-caps (EE), and pre-shower detector in end-caps and has a geometrical coverage up to $\eta \leq 3.0$ .Precise measurement of electron and photon and their separation is possible up to $\eta \leq 2.6$ because the tracker coverage support exists only in this region.

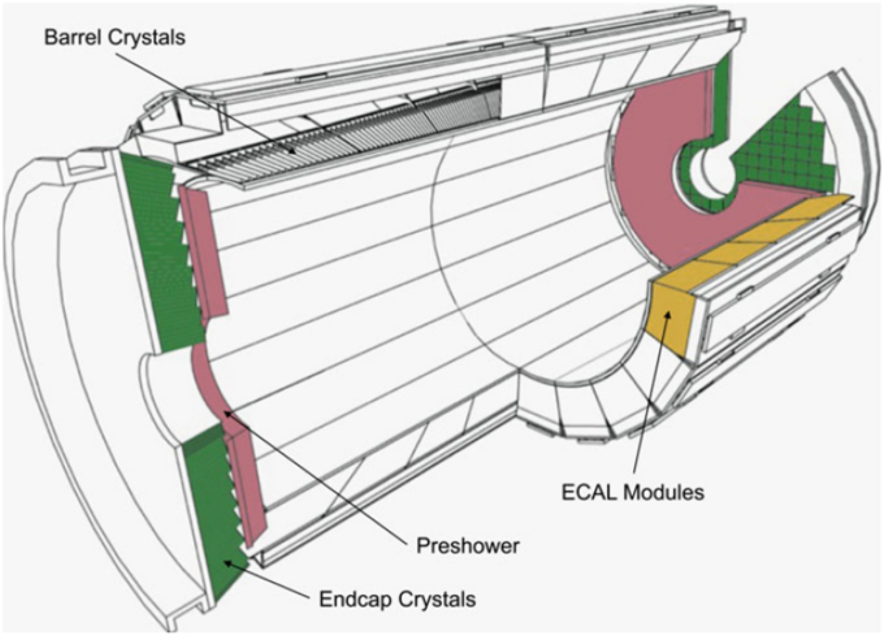

Figure 2.7: Schematic view of the CMS Electromagnetic Calorimeter.

For extra spatial precision, the ECAL also contains pre-shower detectors that sit in front of the end-caps. These allow CMS to distinguish between single high-energy photons (often signs of exciting physics) and the less interesting close pairs of low-energy photons (arising from $\pi^o \rightarrow \gamma\gamma$).

The ECAL is composed of lead-tungstate ($PbWO_4$) crystals, acting both as interaction media and as scintillators, attached to photomultipliers to amplify the relatively small amount of light photons they emit due to incident particle.

The $PbWO_4$ crystals have a short radiation length (0.89 cm), small Moliere radius (2.2 cm), fast scintillation time (80% of the light is emitted within 25 ns), and are radiation hard (up to 10 Mrad).

Figure (2.8) shows one of these crystals, and the crates that hold them, and their disposition in the end-cap.

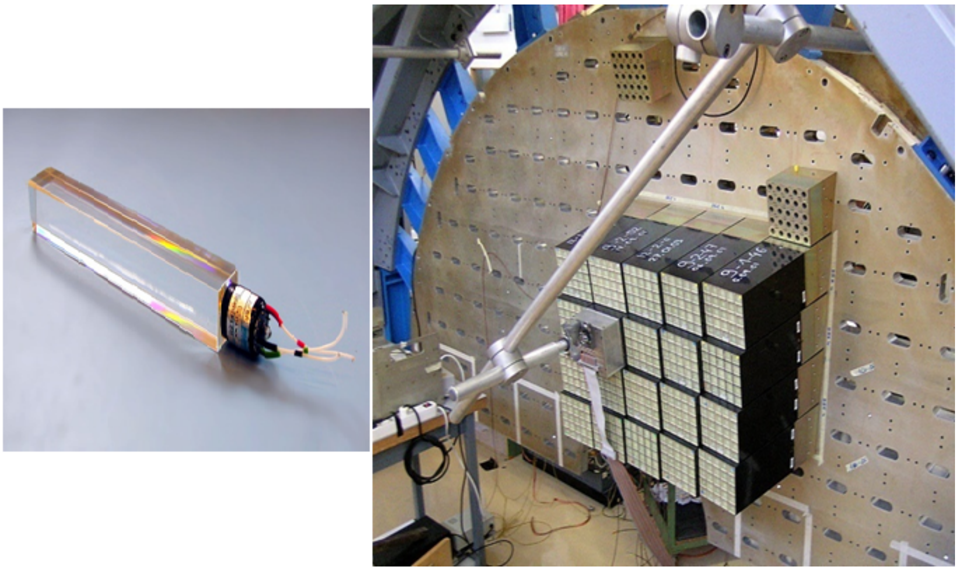

Figure 2.8: Picture of a $PbWO_4$ crystal (left) used in the ECAL with its photomultiplier, and of the end-cap ECAL (right) showing the crates in which the crystals are placed.

The ECAL consists of about 61,000 lead-tungstate crystals in the barrel ($\eta \leq 1.44$) region, and about 7200 crystals each are mounted in the two end-caps ($1.56 \leq |\eta| \leq 3.0$). In the barrel region each crystal has a size of 22x22 mm^2 and is 230 mm long. The crystals are 25.8 radiation length (X_o) in depth and contain most ($\sim$99%) of the electromagnetic shower while the end-cap crystals are 24.7 X_o deep.

The ambient radiation causes the crystals to become opaque and emit less photons which in turn implies a constant need for re-calibration of the detectors.

2.2.4 The Hadronic Calorimeter

The CMS **H**adron **CAL**orimeter (HCAL) [33] will play a crucial role in search for new physics at the LHC. HCAL is particularly important for the measurement of hadron jets and exotic particles resulting in apparent missing transverse energy, it uses strong interactions between the hadrons and the material to create hadronic cascades. Hadronic showers start to develop later and have larger longitudinal and lateral dimensions than electromagnetic ones, so it requires longer detectors.

The HCAL consists of three components the **H**CAL **B**arrel detector (HB), the **H**CAL **E**nd-cap detector (HE), and the **H**CAL **F**orward detector (HF). Figure [2.9] shows the location of the CMS HCAL.

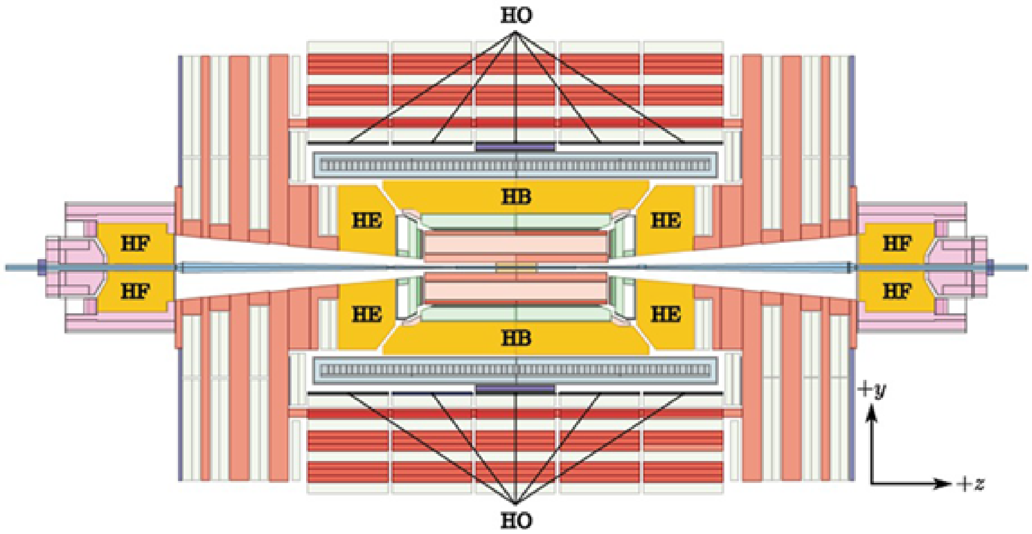

Figure 2.9: Cross sectional view of the CMS detector in $y-z$ projection with the components of the hadronic calorimeter labeled.

The HCAL consists of layers of dense material (brass or steel) interleaved with tiles of plastic scintillators, read out through wavelength shifting optical fibers by photo-sensors in the barrel and end-cap regions.

The HCAL is composed of an alternation of 16 layers of absorbers, made out of 40 to 70 mm thick steel plates and 50 to 56 mm thick 70% Cu and 30% Zn alloy plates, and 3.7 to 9 mm thick plastic scintillators. The barrel HCAL is divided into 72 segments in ϕ and 16 η sectors while the end-cap HCAL has 36 and 72 ϕ segments for the inners and outers rings respectively, and 14 η sectors.

2.2.5 CMS Magnetic Field

To measure the momentum of charged particles, magnetic field is needed to bend their trajectories, the relation between the radius of curvature and the transverse momentum is:

$$R[m] = \frac{p_T[GeVc^{-1}]}{0.3B[T]} \tag{2.2}$$

Where B is the magnetic field intensity, by inverting the pervious relation the transverse momentum of the charged particles can be obtained. CMS has optimized for a long solenoid superconducting coil [34]. The intensity of the field is of 3.8 T inside the solenoid and typically 2T outside the solenoid. Placing the calorimeters inside the magnet improves the energy resolution as particles have less distance to travel through before reaching them. Figure [2.10] shows a map of the magnetic field over CMS detector.

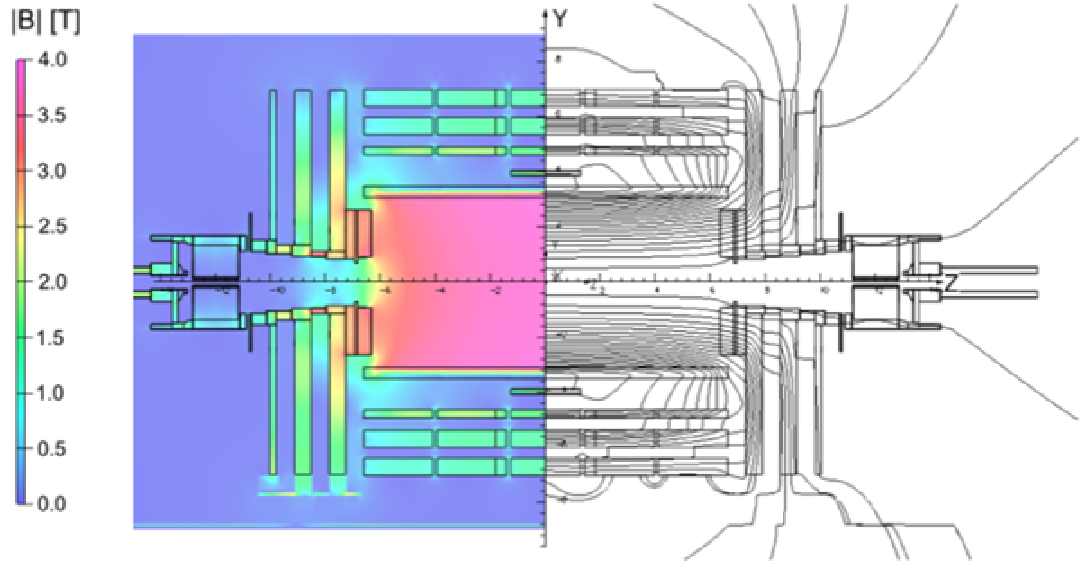

Figure 2.10: Field map of the magnetic field of CMS measured using cosmic rays [35].

2.2.6 Muon System

Muon detection is an important aspect of any experiment of particle physic, especially CMS, which is one of the main design objectives of the detector that is obtaining a high precision muon momentum measurement, given its key role both in New Physics searches and in Standard Model measurements.
Muons can be identified by the large penetrating power and the relevant parameters to be measured very precisely are energy and momentum. We will first describe the interactions between the particles and the detectors, and then describe the different detector technologies used in CMS muon system.

Particle Detection in Gas Detectors:

Particles passing through matter [36] can interact with the medium through multiple processes. Muons energy losses, are dominated by the Coulomb interaction with the electrons of the medium. Figure [2.11] shows the average energy loss dE per length dx is given by normalized to the density of the detector material as a function of the $\beta\gamma$ parameter for muons passing through copper.

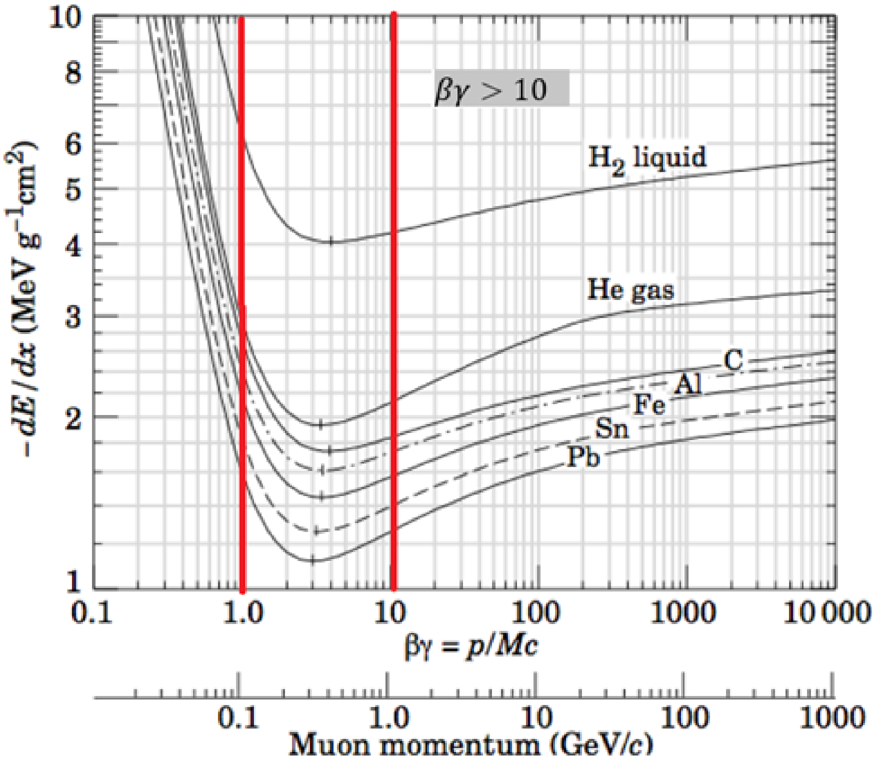

Figure 2.11: Mean energy loss per unit length of muons in the traversed material, normalized to the density of the medium as a function of $\beta\gamma$ parameter [36].

For particles in the $0.1 \leq \beta\gamma \leq 10,000$ range, the energy losses have been quantified by Bethe as follows [36]:

$$-\langle\frac{dE}{dx}\rangle = Kz^2\frac{Z}{A}\frac{1}{\beta^2}\left[\frac{1}{2}ln(\frac{2m_ec^2\beta^2\gamma^2T_{max}}{I^2}) - \beta^2 - \frac{\delta(\beta\gamma)}{2}\right] \quad (2.3)$$

where z is the charge number of the particle, Z, and A are the atomic number and atomic weight of the absorber, m_e is the electron mass, T_{max} is the maximum energy that can be transferred during a collision, I is the mean excitation energy, characteristic of the absorber material, $\delta(\beta\gamma)$ is an ultra-relativistic correction, and $K = 4\pi N_A r_e^2 c^2 m_e$, r_e being the classical electron radius, and N_A is the Avogadro's number.

As illustrated in figure [2.11] at low energies $\beta\gamma < 1$, the stopping power is large, that is because in this case the speed of the particles traversing the detector material is comparable to the speed of the atomic electrons, which effectively slows down the speed of the incident particle. The opposite effect occurs at high energies $\beta\gamma > 10$, the incident particles becomes ultra-relativistic they create a temporary polarization of the detector material (Cerenkov Radiation), and so reducing the energy losses.In the range between the two red lines ($1 < \beta\gamma < 10$), energy losses are minimal, the incident particles having this energy range are characterized by a specific name: **M**inimum **I**onizing **P**articles (MIP). Detectors must be tested in this specific region to ensure their detection capabilities and to calibrate their response.

It is important to realize that the total energy of incident particles is not used to ionize the detector material, but there is also what is called secondary ionization, such as Auger effect, during which an electron from higher orbitals takes the place of the ejected electron, emitting a photon. This photon can either escape and remain undetected, or in most cases, be absorbed by another electron causing a double ionization, The average number of ionization (primary and secondary) by unit of length n is given by:

$$n = \frac{1}{W}\langle\frac{dE}{dx}\rangle \tag{2.4}$$

Where W is the mean energy needed to ionize the material. It is important to emphasize that energy losses are stochastic processes. Therefore, particles do not leave behind a constant trail of ionization, but rather localized energy depositions, resulting in the detection of multiple hits inside one detector. The deposited energy follows a Landau distribution where the most probable value is given by Bethe's formula review in eqation [2.3].

Performance parameters:

Four parameters characterizing the detectors, especially muon system are of importance in CMS: the *spatial resolution*, the *temporal resolution*, the *detection efficiency*, and the *rate capability*, each of which plays an important role in the reconstruction of the events.

- **Spatial Resolution**: The spatial resolution is the error on the position's measurement made by the detectors. It yields the resolution on the momentum when reconstructing the track, as hits are used to measure the bending radius of the trajectories. The momentum being the key quantity used to analyze events, it is important to ensure a good spatial resolution on the hits' position, of the order of 250 to 500 μm in the CMS muon spectrometer. For gaseous detectors, the spatial resolution will vary with the placement and spacing of the electrodes. Some detectors only measure one direction, neglecting the other. This will often be the case in muon chambers as the area to cover is quiet large, and costs must stay reasonable.

- **Temporal Resolution**: The time resolution is important in order to correctly assign particles to a certain Bunch Crossing (BX). With the high frequency at which the LHC runs, it is important to determine during which collision a certain particle was created. For detectors close to the interaction point, the **T**ime **O**f **F**light (TOF) is relatively short. However, muons reaching the muon system can have a TOF up to 40 ns. This means that particles from one interaction reach the outer detectors while another collision already took place. To unambiguously assign an event to a BX, the time resolution must be less than to 5 ns.
- **Detection Efficiency**: The detection efficiency ϵ is the percentage of particles passing through the chamber and which are detected. CMS requires all detectors to have a minimum efficiency of 95%.
- **Rate Capability**: The rate is the maximal flux of particles under which the detection efficiency remains above 95%. Parts of the gaseous detectors remain unusable for a certain amount of time after the avalanche process. In order to increase the system's efficiency, the rate capability should be of the order of the particles flux traversing the detectors. Detectors in the most forward region of CMS should be able to sustain rates of the order of 1 kHz cm^{-2}.

In the following subsections we will describe the CMS muon system in details. Currently, the CMS muon system is composed of three different types of gaseous detectors: **D**rift **T**ubes (DT), **C**athode **S**trip **C**hambers (CSC), and **R**esistive **P**late **C**hambers (RPC).

Deposition of the detectors:

Like all the CMS detectors, the muon system is divided into two regions: the barrel ($|\eta|$ <1) and the end-caps (1< $|\eta|$ <2.4). The chambers are regrouped into stations attached to the wheels of CMS. The barrel stations contain DTs (identified by MBn) and RPCs while the endcaps stations hold CSCs (identified by MEx/y) and RPCs (identified by REn), as represented in figure [2.12]. For financial reasons, the RPCs were not installed for the LHC's start-up in the (1.6< $|\eta|$ <2.4) region where only CSCs are present.

The barrel is composed of 5 wheels on which 4 layers of detectors are attached, each divided into 12 stations along ϕ. The end-caps have 4 layers of detectors divided into 1, 2 or 3 rings partitioned into 36 or 72 stations that overlap to ensure maximum efficiency. Figure [2.12] shows the first station of the muon end-cap, ME1. The inner ring, called ME1/1 is hidden by the so-called nose, in black. The two outer rings, ME1/2 and ME1/3 are well visible. In ME1/2, we can observe the overlap between the chambers.

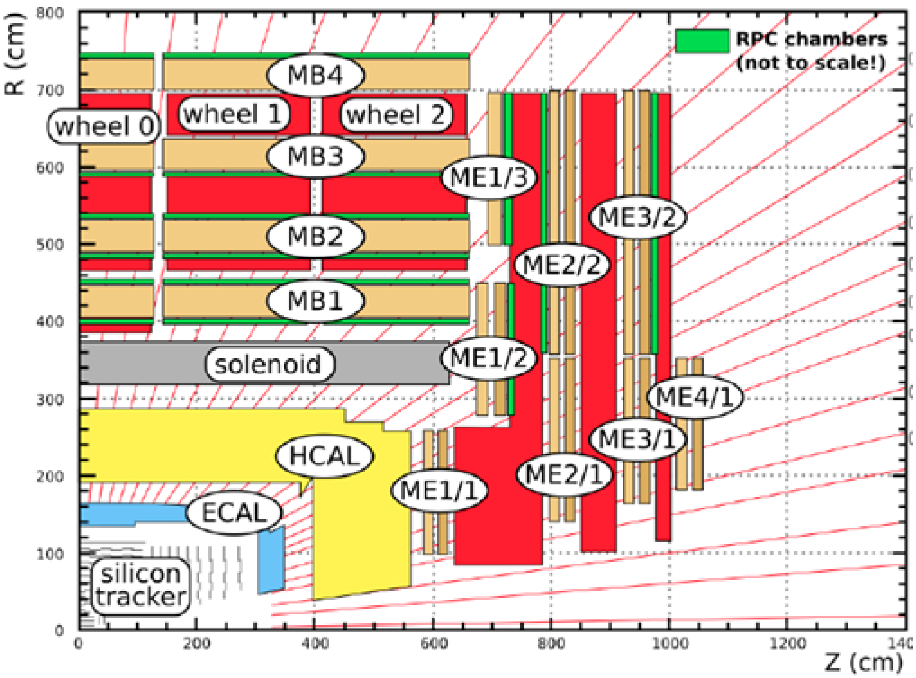

Figure 2.12: Disposition of the muon chambers inside CMS. MBn refer to DTs, MEn to CSCs and the green lines to RPCs.

The use of two different kinds of detectors in each station ensures that the system meets the required detection efficiency for muons imposed by CMS. This redundancy is crucial to select and reconstruct events with high momentum muons in the final state, like the signature of the Brout- Englert-Higgs boson's decay and many processes of new physics, including super-symmetry.

Drift Tubes:

Drift Tubes [37] are rectangular parallelepiped detectors composed of an anode wire stretched between two cathode strips as represented in figure [2.13]. The chambers are 2.4 m long by 13 mm height by 42 mm wide. A strong electric field (of the order of 1.5 kV cm^{-1}) is formed by applying a high voltage difference between the electrodes, causing the electrons and ions to drift into the gas, and provoking avalanches near the anode. The two electrodes placed near the anode help flatten the electric field and improve the charges' drift.

Four DTs are assembled to create a Super Layer (SL), and two or three SLs compose a DT module. Each SL has a spatial resolution of 100 μm in the direction perpendicular to the wire. To improve global precision, two SLs are used to measure the ϕ coordinate and sometimes one additional SL is used to measure η. DT modules have a time resolution of 3 ns. Their rather large size limits their rate capabilities, explaining why they are only present in the barrel where particles' fluxes are lower (<10 Hz cm^{-2}).

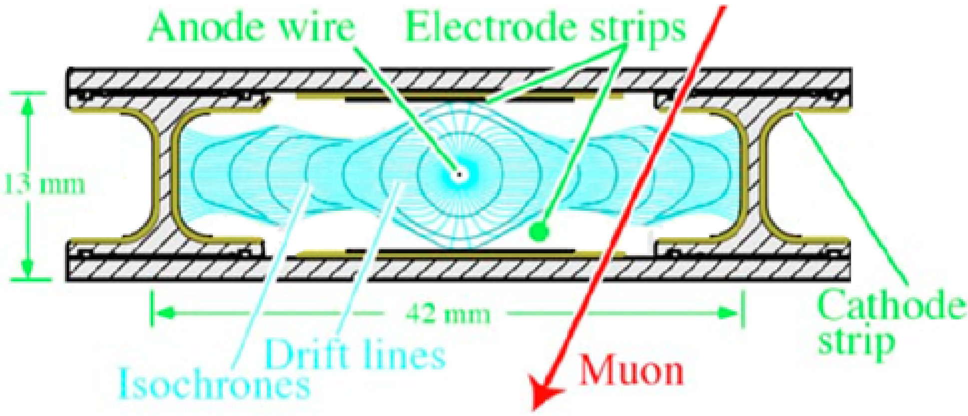

Figure 2.13: Schematic view of a drift cell along with the electric field line.

Cathode Strip Chambers:

Cathode Strip Chambers [38] are trapezoidal multi-wire proportional chambers placed in the end-caps of CMS. Multiple anode wires (about 1000 spaced by 3.2 mm) are stretched radially in the chamber above perpendicularly placed cathode strips (typically 80 separated by a pitch of 8.4 mm on the narrow side and 16 mm on the large side) as depicted in figure [2.14] .

As for the DTs, an electric field is formed between the wires and the strips, accelerating the electrons and forming the avalanches near the anodes. By reading-out both electrodes, the CSCs provide a measurement of both coordinates.

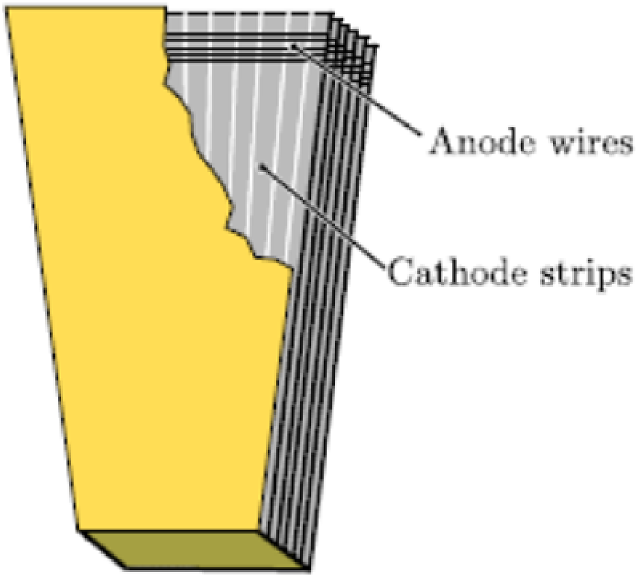

Figure 2.14: Schematic view of cathode strip chamber.

One CSC module is made out of six chambers put together (7 cathode planes and 6 wire planes). Due to the large number of readout channels in these modules, the spatial resolution is as good as 33 μm for ME1/1 and ME1/2, and 80 μm for the other stations. The time resolution for one cathode plane is 11 ns that can be brought down to the order of 5 ns when combining the measurements of all the planes. The largest CSC modules, ME2/2 and ME3/2, are 3.4m by 1.5m.

Resistive Plate Chambers:

Resistive Plate Chambers (RPCs) [39] are gaseous detectors used in both barrel and end-cap regions. Their spatial resolution is limited, but their time resolution is very good, about 2 ns, a shorter time than the 25 ns LHC BX. Therefore RPC detectors are used to provide trigger decisions because of its fast response and good time resolution. The resistive plate chamber used in CMS experiment consists of two layers of gas gaps with a sheet of segmented copper readout strips sandwiched between them as shown in figure [2.15].

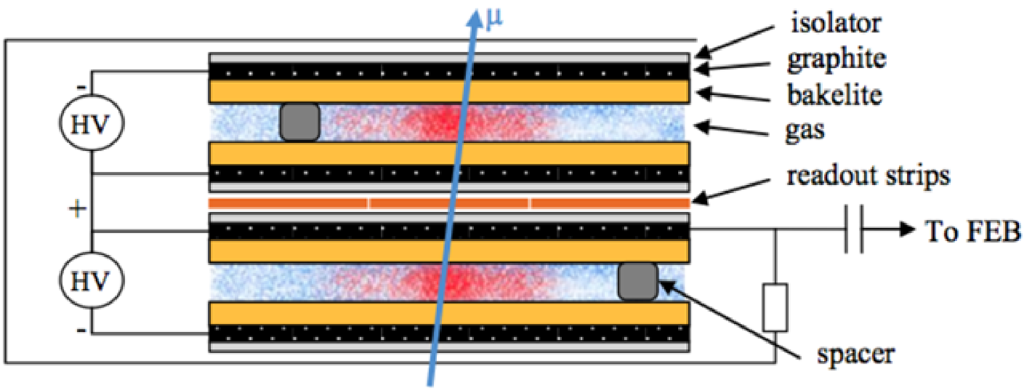

Figure 2.15: Schematic view of resistive plate chambers.

A gas gap (few mm thick) is made of two sheets of high resistive Bakelite, a high-resistivity plastic material, which acts as the electrode with graphite coat outside of them. Within the resistive plate chamber the electric field is uniform. The sheet of the readout strips is put in the chamber, centered on the bottom gap separated from the graphite layers by an insulating PET (polyethylene terephtalate) film, to read out the signals. There are 32 strips running the length of the chamber but they are broken up lengthwise into three sections for the readout purpose.

The RPC is a detector utilizing a constant and uniform electric field produced by two resistive parallel electrode plates. The gap between these two plates filled with a gas mixture of Freon and isobutene. When a charged particle passes through the gas, the gas atoms will ionize and form electron-ion pairs. The electron goes to the positive electrode and discharge is originated by intense electric field. The discharge was prevented from propagation through the whole gas by the quenching properties of the gas mixture. The geometrical layout of the RPC chambers depends on their position. In the barrel region, six layers of RPCs are there: four of them are attached to each side of the MB1 and MB2 DT chambers, the other two attached to the inner side of MB3 and MB4. In the end-caps, four disks of trapezoidal RPC are attached to the CSCs.

2.3 Data Acquisition System

The CMS trigger and the **D**ata **A**cquisition **S**ystem (DAQ) [40] is designed to overcome the unprecedented interaction rate. The interval between BX is 25 ns, corresponding to a frequency of 40 MHz. Approximately 25 simultaneous p-p collisions occur each crossing at the nominal design luminosity of $10^{34}\mathrm{cm}^{-2}\mathrm{s}^{-1}$. With the extremely high rate of out coming events, it is impossible to store such a large amount of data, a drastic rate reduction has to be achieved. This task is performed by the trigger system, which is the start of the physics event selection process.

The rate is reduced in two steps corresponding to the **L**evel-1 Trigger (L1), which is based on highly customized fast electronics and **H**igh- **L**evel **T**rigger (HLT) [41], which is implemented on a large cluster of commercial processors (Event Filter, Event Filter Farm).

Various components of DAQ and triggers system for CMS are shown schematically in figure [2.16].

The L1 trigger has access only to coarsely segmented calorimeter and muon detector information in order to identify various physics candidate objects. At this stage isolation criteria is applied without any information from the tracking system. The rejection and acceptance by trigger is based on the characteristics of the trigger objects. These trigger objects or candidates are identified from the detector information. The data from the front end electronics of various sub detectors are put into 107 channels with a latency time (or dead time) of 3.1 μs. This latency time is equivalent to 128x25 ns beam crossing at the designed luminosity. After an event gets accepted by the L1 trigger, about 700 Front End (FE) modules holds the stored event data, each carrying about 1-2 kB of data per L1 trigger accepted event. The L1 accepted signals (102kHz) and raw readout data are sent to a computer farm through a temporary storage buffer.

The next level is HLT which applies a reduction factor of 1000 to the output of L1 trigger. The full resolution and granularity of the detector is used to achieve such a large rejection factor. At this stage the information from tracker is also used for isolation and trigger selection and it is as sophisticated as at the time of online processing of the data. It essentially combines the traditional L2 and L3 trigger components and allows a coherent use of HLT algorithms for multiple physics channels. Here the software used are the same as will be used in online analysis of the data.

This requires fully programmable commercial processors (EF farms) for the running of HLT algorithms with a mean time of 10 ms per event along with the maximum input rate of 100 kHz. The trigger selection are implemented as (*trigger path*) where a trigger path is a set of algorithms which reconstruct one or more physics candidates and applies selection criteria to these reconstructed candidates and their various isolation and kinematical quantities. If the event passes one or more of these paths, the event gets accepted and stored for analysis.

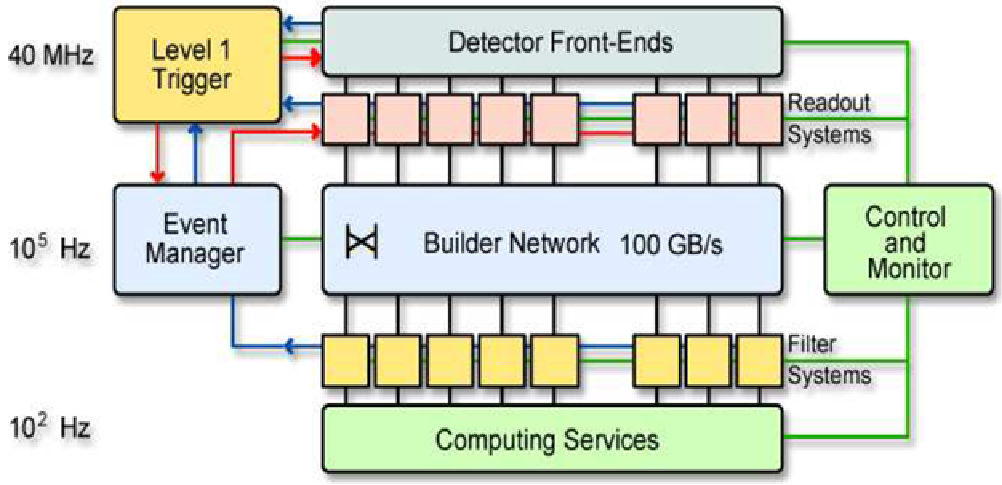

Figure 2.16: A layout of CMS architecture of Data Acquisition System and Trigger and various important components.

To sum up CMS is a multi-purpose experiment that can shed light on many of today's fundamental open questions in physics. New detector developments as well as trigger and data acquisition schemes contribute to make CMS a highly competitive apparatus for the exploration of the high-energy physics frontiers.

Chapter 3

Event Generation and Analysis

3.1 Monte Carlo Event Generators

To discover new particles at LHC, **M**onte Carlo (MC) events are needed to compare the signal events to background events, and observe any excess over background. So MC event generation is an essential tool for the search of new particles.

Monte Carlo event generators are based on **M**atrix **E**lement (ME) theoretical calculation, their task is to perform, initial composition, initial state radiations, hard scattering, resonance decays, final state radiations, Multi-Parton interactions, and hadronization. There are different categories of event generators that are intended to do only hard matrix element calculations without showering and hadronization.

Since the LHC is a hadron collider based on proton-proton collisions, the compositeness of the proton has to be taken into account; the proton consists of valence quarks, sea quarks, and gluons, these entire constituents share the proton momentum, so the center of mass energy is distributed over the parts of each proton which is also called partons. If x_1 and x_2 are the fractions of the parton momentum with respect to the proton momenta, the center of mass energy of two interacting partons is given by:

$$\sqrt{\hat{s}} = \sqrt{x_1.x_2}\sqrt{s} \tag{3.1}$$

where $\sqrt{s}$ is the center of mass energy of the two colliding protons. But the exact momentum of the two partons is unknown, so it is described by a **P**arton **D**istribution **F**unctions (PDFs) which are statistical distributions of the parton momenta at proton-proton colliders. The predicted cross section of a process at hadron colliders depends on the used PDF set, meaning that it can different for different PDFs.

There are several MC generator programs that generate events in protonproton, proton-antiproton, electron-positron, electron-proton and electron-electron collisions. Among these the general purpose MC generators PYTHIA [42].

In MC generators the treatment of colored partons to colorless hadrons is based on phenomenological models. PYTHIA uses String Model for event generation. In this model the final state q and q partons move apart from the production vertex, as they move apart, their potential increases and creates new qq pairs, if they have enough energy, further pair creation proceeds in the same manner. In this model, the process is assumed to proceed until only on-mass-shell hadrons remain. Figure [3.1] shows the schematic picture of string model of hadronization process.

On the other hand, Madgraph5 [43] event generator is hard matrix element generator, it can calculate the cross section at **L**eading **O**rder (LO) accuracy and **N**ext to **L**eading **O**rder (NLO) accuracy. Madgraph5 can linked to PYTHIA, or HERWIG [44] for event showering and hadronization, and could be also linked to fast detector simulation tools for detector response simulation as described below.

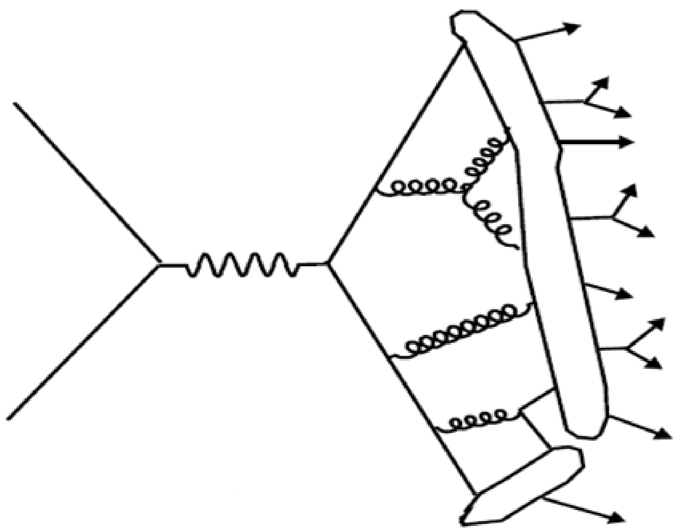

Figure 3.1: Hadronization using String Model in Monte Carlo event generators.

3.2 Signal Properties

In this thesis we will focus on the muon compositeness in the phase II of LHC run at center of mass energy $\sqrt{s} = 14$ TeV with the CMS detector, the considered channel is the single production of excited muon via CI and decay via neutral-current decay, in partcular $qq \rightarrow \mu\mu^* \rightarrow \mu\mu Z \rightarrow 4\mu$ so the final state will be four muons as shown in figure [3.2] and this will be the signature that we are looking for at the CMS detector, Although the branching ratio of this decay mode is much smaller than γ-mediating process the four muon final state gives out less background than $\mu\mu\gamma$.

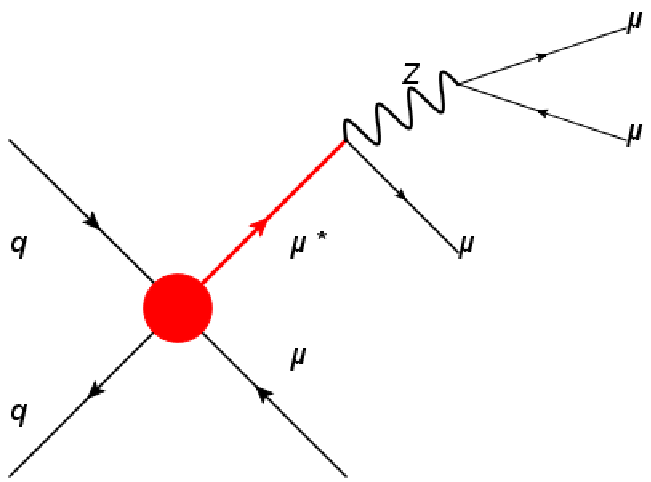

Figure 3.2: Decay channel considered, four muons will be the signature of excited muon.

Before the comparison between data and SM background, we present a generator-level study of signal events. The characteristic distributions are studied, showing the expected kinematics of the final states and their dependence on the excited muon mass.

Signal samples are generated at LO aacuracy using PYTHIA 8.2 MC event generator with a mass range 0.5 to 5 TeV with a step of 0.5 TeV, and a compositeness scale Λ= 10 TeV using *CTEQ6L1* PDF. Although signal samples are generated at Λ= 10 TeV one can easily scale to different Λ as long as we use the correct branching ratios, this effect is illustrated in figure [3.3] which shows the cross section of the signal as a function of excited muon mass for different values of Λ, as it clear the cross is inversely proportional to the compositeness scale and for different values of Λ the relation is linear meaning that the kinematic distributions and results could be scaled to an value of Λ.

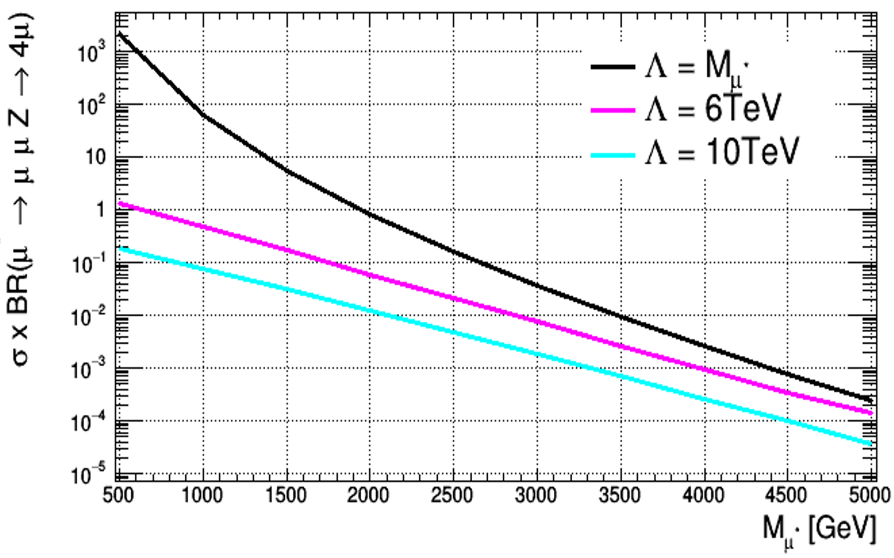

Figure 3.3: Signal cross section x branching ratio (σ x BR) in fb^{-1} depending on the excited muon mass for different Λ values.

Firstly to reconstruct the excited muon mass, three muon are needed to perform this process, two of them are oppositely charged and their invariant mass are close to the Z mass ($60 < M_{Z1,Z2} < 120$ in [GeV]). So by reconstructing the Z boson mass, one muon is needed to reconstruct the mass of μ^*, but there are two indistinguishable options namely μ_{CI} (the companion of μ^*) and μ_{decay} (which results from μ^* decay). From these two options we can form two invariant mass plots, the minimum invariant mass $M_{min}^{3\mu}$, and the maximum invariant mass $M_{max}^{3\mu}$ in increasing order of mass. Figure [3.4] shows the $M_{min}^{3\mu}$ and $M_{max}^{3\mu}$ respectively for mass points (0.5TeV, 1.5TeV, 2.5TeV, 4TeV, and 5TeV). It can be seen that the mass peak from the excited muon is well reconstructed for low invariant masses if $M_{min}^{3\mu}$ is used and for high invariant masses if $M_{max}^{3\mu}$ is used. But these two options rise the problem that which of the two distributions is better for optimization of the selection procedure of the signal, but by forming a 2D plot of the two invariant masses can solve this problem. This application leads to an *inverse L shape*, that is if the excited muon mass is reconstructed by using $M_{min}^{3\mu}$ it leads to a vertical leg around the simulated mass while a reconstruction via $M_{max}^{3\mu}$ leads to a horizontal leg around the simulated mass.

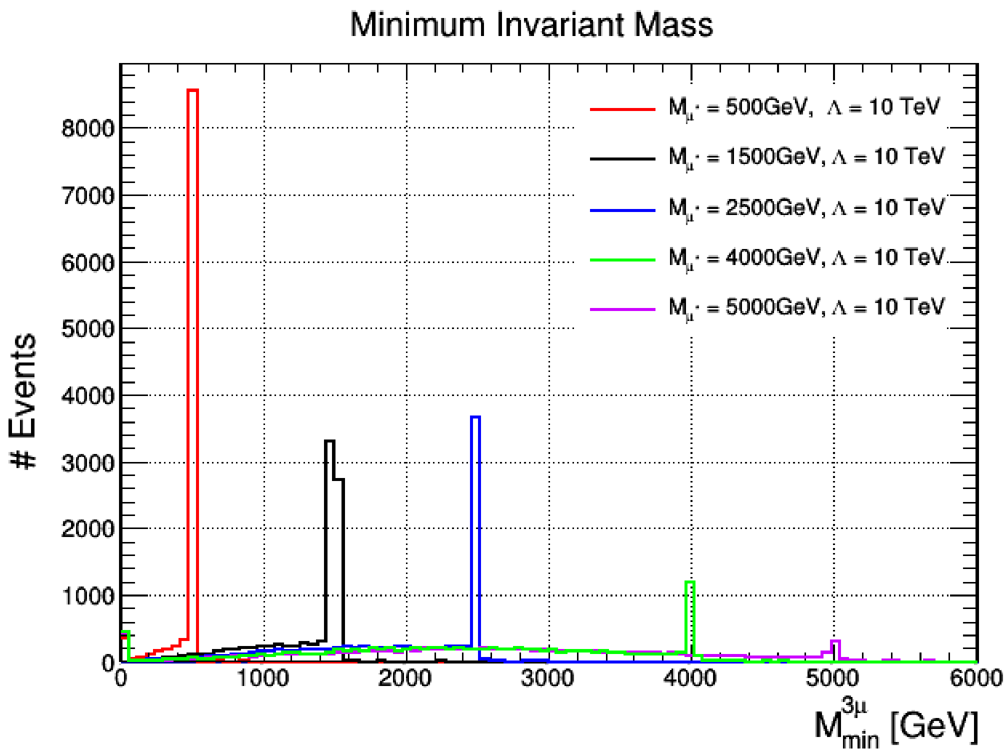

(a)

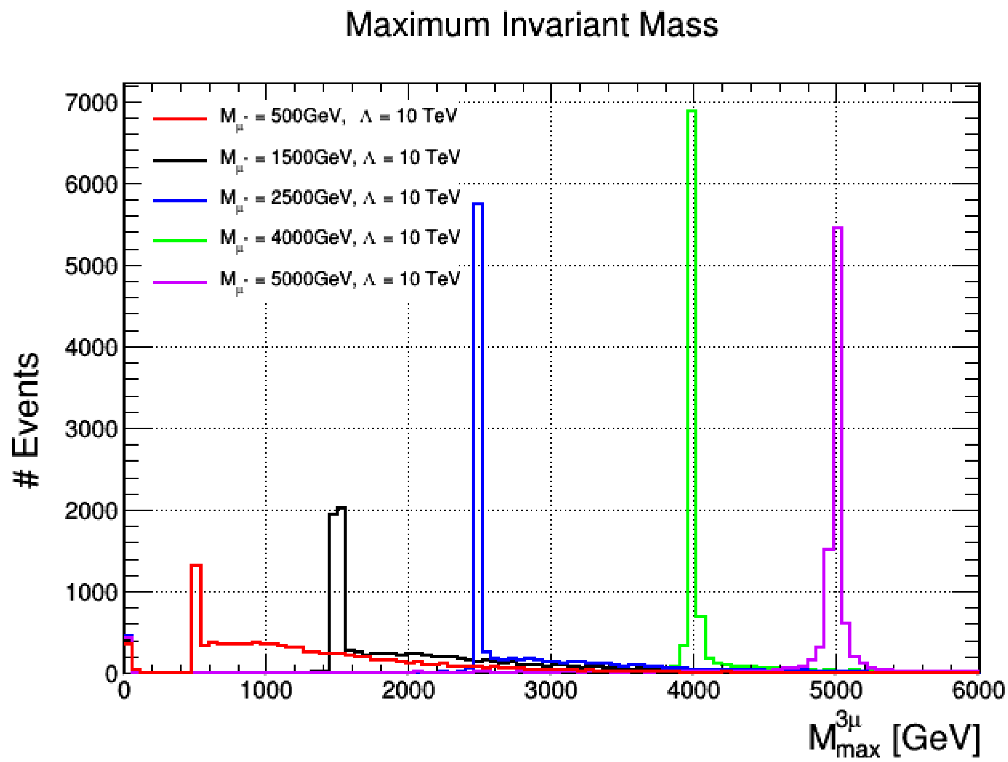

(b)

Figure 3.4: (a) Minimum Invariant mass at generator level, and (b) Maximum Invariant mass at generator level.

Figure [3.5] shows the L-shape plot for different simulated mass points. After performing detector simulation the width of the "L" can be expected to have a much larger width because of the muon momentum resolution of the detector

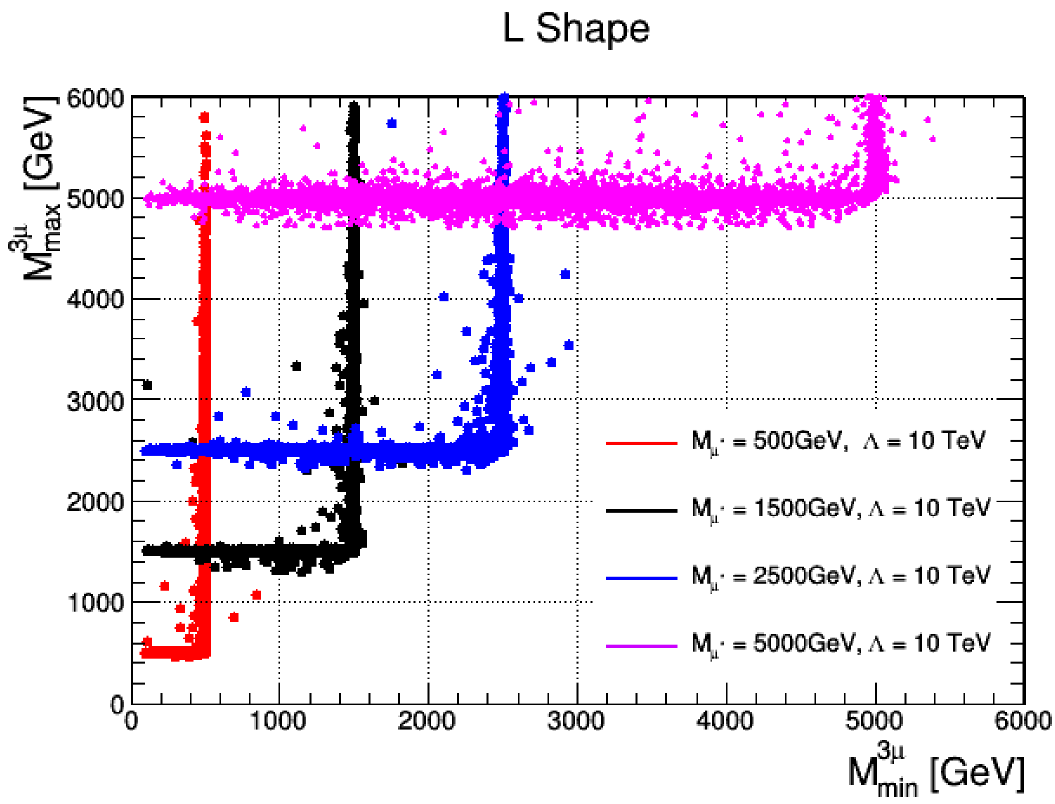

Figure 3.5: 2D minimum-maximum invariant mass plane, also called L-shape diagram.

It is very important to study the properties of each one of the four muons. Two of them μ_{CI} and μ_{decay} are expected to have high values of transverse momentum, since μ_{CI} is coming from hard interaction and μ_{decay} is coming from the decay of heavy particle. The two other muons that are coming from the decay of Z-boson are expected to have soft transverse momentum spectrum. Figure [3.6] illustrates the transverse momenta p_T of the four muons in increasing order for different mass points, where the *leading muon* is the highest p_T muon. The leading muon of the mass point M_{μ^*}=500 GeV have $p_T \geq 50$ GeV, while higher masses have have higher values of p_T. It is observed also that the two leading muons have comparable p_T. The two slowest muons have a softer spectrum, even for high μ^* masses.

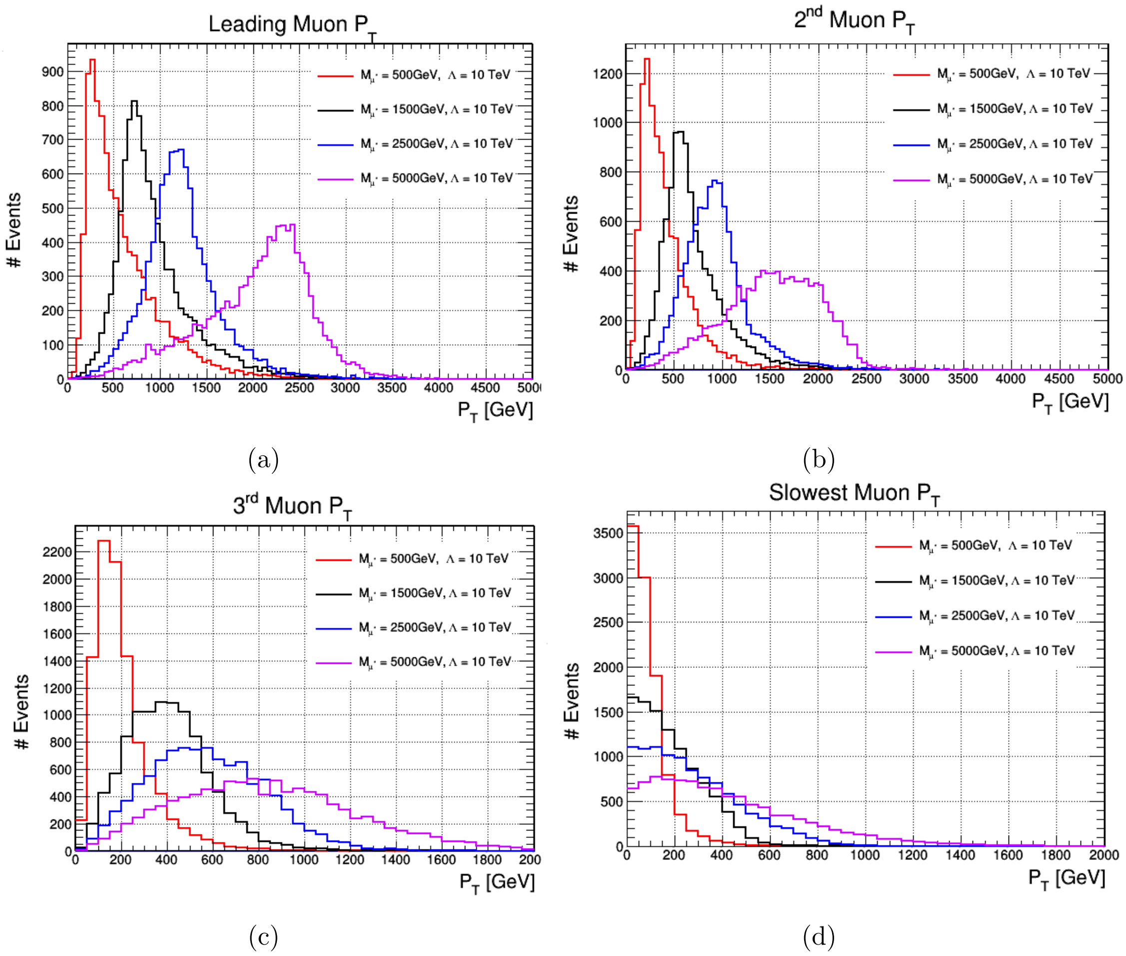

Figure 3.6: Leading (a), second to leading (b), 3^{rd} (c) and slowest (d) muon transverse momenta p_T at generator level.

One important step in studying the signal events is to study the Z particle, as we will construct the μ^* mass after reconstructing Z. So figure [3.7] shows the invariant mass of the reconstructed Z-boson and its transverse momentum p_T^Z for different values of μ^* mass. It can be seen that p_T^Z increases for higher masses which leads a small angle between the decay products. This effect is shown in figure [3.8] where ΔR between the decay products of Z is plotted and $\Delta R = \sqrt{\Delta\eta^2 - \Delta\phi^2}$, where $\Delta\eta$, and $\Delta\phi$ are the pesudorapidity and azimuthal angle differences respectively between the two muons.

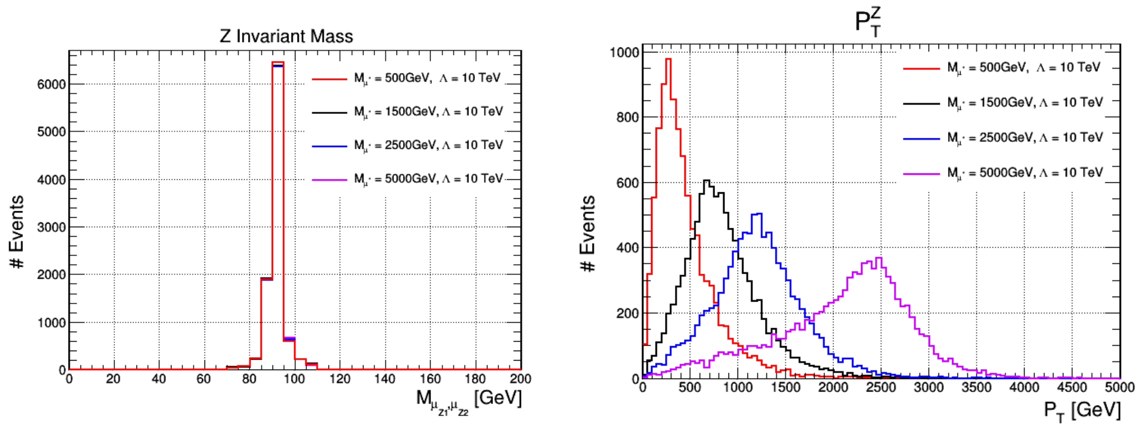

(a) (b)

Figure 3.7: (a) The invariant mass of the Z particle for different mass points at generator level. (b) The transverse momentum of the Z particle at generator level.

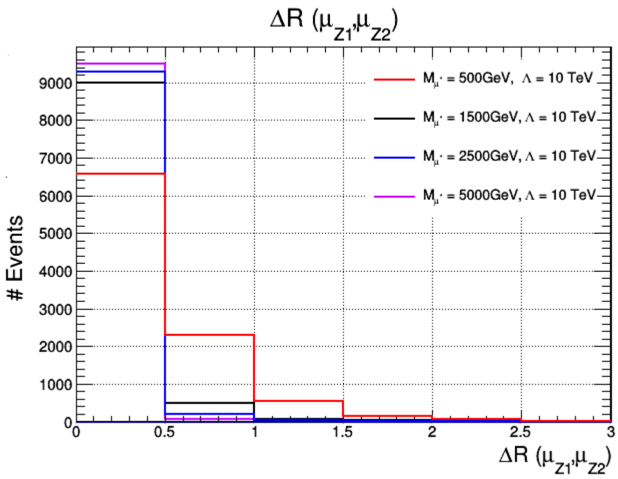

Figure 3.8: ΔR between the decay products of Z particle.

A further investigation of signal properties is given in figure [3.9], where the invariant mass of the μ_{CI} and μ_{decay} which forms what we will call from now on the Z_{veto} is shown. This distribution will discriminate the signal against background and after applying a cut on this invariant mass will enhance the signal over background ratio. In the same figure the ΔR between μ_{CI} and μ_{decay} where it is observed that its value is large compared to the ΔR between the decay products of Z, consequently it cannot be used as a discriminating variable.

Table [3.1] lists the cross section x branching ratio of excited muon to give 4 muons final state.

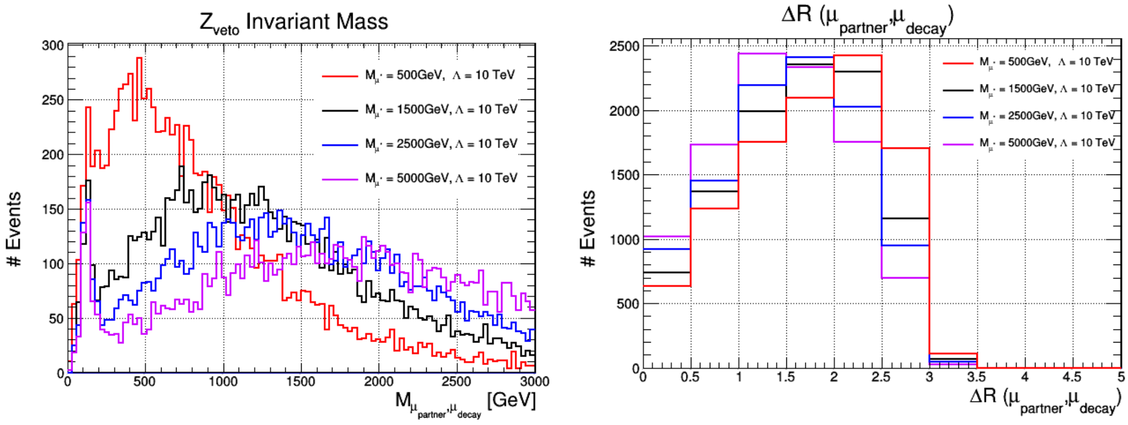

(a) (b)

Figure 3.9: (a) The invariant mass of Z_{veto} the as function of the excited muon mass (b) ΔR between μ_{CI} and μ_{decay} as function of the excited muon mass.

Mass [GeV]	σxBR($\mu\mu^* \to 4\mu$) [fb]	Number of Events
500	1.78x10^{-1}	10000
1000	7.50x10^{-2}	10000
1500	3.07x10^{-2}	10000
2000	1.23x10^{-2}	10000
2500	4.82x10^{-3}	10000
3000	1.86x10^{-3}	10000
3500	7.00x10^{-4}	10000
4000	2.61x10^{-4}	10000
4500	9.59x10^{-5}	10000
5000	3.46x10^{-5}	10000

Table 3.1: List of the cross section x branching ratio of signal events for mass points considered.

3.3 Background Expectation

Various Standard Model processes can give the same final state as these signal events. In real data, if the excited muon exist both signal events (4μ final state) and SM processes that give 4μ will be produced at LHC (strictly speaking huge number of events that give a variety of final states), so to discriminate signal events from the huge number of events we have to identify SM processes that give 4μ final state, which will be considered as background events.

Various SM background processes were simulated at LO accuracy at $\sqrt{s}$ = 14 TeV using MadGraph5 interfaced with PYTHIA8 for haronization and showering, and then passed to Delphes3.3 [45] for CMS detector simulation.

Delphes is a framework, performing a fast multipurpose detector response simulation. The simulation includes a track propagation system embedded in a magnetic field, electromagnetic and hadron calorimeters, and a muon identification system. Physics objects that can be used for data analysis are then reconstructed from the simulated detector response. Although Delphes can simulate the CMS detector very well, it is not meant to be used for advanced detector studies, it intended for phenomenological studies as considered in this thesis.

Table [3.2] lists the background for this analysis and the simulated number of events.

Process	σ [pb]	Number of Events
$pp \to$ zz $\to 4\mu$	1.16x10^{-2}	750000
$pp \to$ zz $\to 4\tau$	1.16x10^{-2}	800000
$pp \to$ zz $\to 2\mu 2\tau$	2.31x10^{-2}	500000
$gg \to$ zz $\to 4\ell$	1.81x10^{-4}	500000
$pp \to t\bar{t}$z	7.08x10^{-1}	500000
$pp \to$wwz	9.41x10^{-2}	500000
$pp \to$wzz	2.98x10^{-2}	500000
$pp \to$zzz	1.03x10^{-2}	500000

Table 3.2: Standard Model background samples, cross section, and simulated number of events.

The way how these background processes can lead to a four lepton final state is summarized below:

1. **pp $\to$ zz $\to 4\ell$:** This is the dominate background for analyses with a four muon final state. It contributes about 90% of the background expectations. The Z boson could decay to two muons 2μ, or decays to tau-leptons τ and the tau decay subsequently to muon and neutrino. Figure [3.10] shows the corresponding Feynman diagrams for this background.

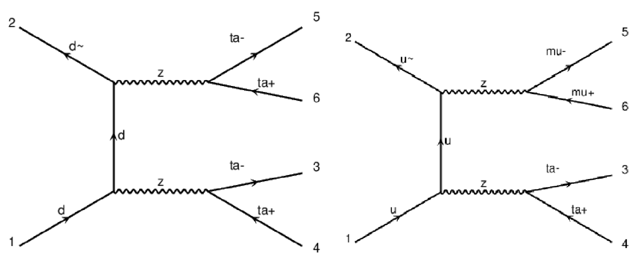

Figure 3.10: Example Feynman diagrams of the dominate background process.

2. **gg → h → zz →4ℓ :** The decay of the Standard Model Higgs boson to two Z-bosons and subsequently to four leptons can also result in a four muon final state [46]. The Higgs boson can be produced in different ways, the process with the highest cross section is the gluon-gluon fusion shown in figure [3.11].

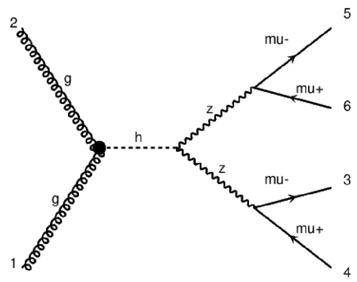

Figure 3.11: Feynman diagram of the gluon-gluon fusion.

3. **t$\bar{t}$z :** This is the second dominate background process. Figure [3.12] illustrates the production of this process. The top quark could decay to b-quark and a W± boson, which subsequently decays to a muon and a neutrino, while the Z boson decays to di-muon and a four muon final state will be formed.

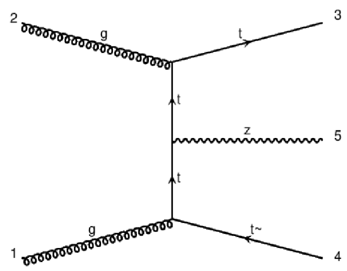

Figure 3.12: Feynman diagram of $t\bar{t}$z, the figure illustrates different production mechanisms.

4. **WWW, WWZ, ZZZ :** Four muons final state could be also produced by very rare processes such as triple vector production pp → VVV, where V is the Z or the W boson.These processes contribute less than 1% of the background expectations. Figure [3.13] the Feynman diagrams for the triple vector production.

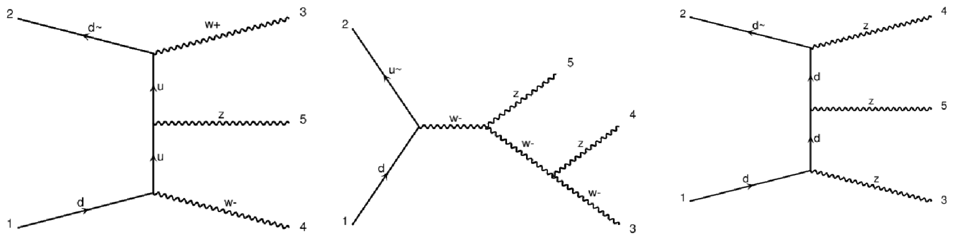

(a) (b) (c)

Figure 3.13: Example Feynman diagrams for (a) WWZ (b) WZZ (c) ZZZ

3.4 Analysis and Results

Finally we come to the crucial point, the comparison between signal and background for different kinematic distributions, signal optimization, and quantify the discovery potential of the excited muon at LHC using CMS experiment. We have studied the signal alone at generator level, so logically the next step is to perform the CMS detector simulation for signal events, so signal events are run through Delphes 3.3 fast simulation software to simulate the CMS detector response.

Mass (μ^*) [GeV]	Weight	Process	Weight
500	5.35x10^{-3}	$pp \to$ zz $\to 4\mu$	4.65x10^{-3}
1000	2.24x10^{-3}	$pp \to$ zz $\to 4\tau$	4.34x10^{-3}
1500	9.20x10^{-3}	$pp \to$ zz $\to 2\mu 2\tau$	1.39x10^{-2}
2000	3.70x10^{-3}	$gg \to$ zz $\to 4\ell$	1.09x10^{-3}
2500	1.45x10^{-3}	$pp \to t\bar{t}$z	4.25x10^{-1}
3000	5.59x10^{-4}	$pp \to$wzz	1.79x10^{-2}
3500	2.10x10^{-4}	$pp \to$wwz	5.65x10^{-2}
4000	7.82x10^{-5}	$pp \to$zzz	6.21x10^{-2}
4500	2.88x10^{-5}	———	———
5000	1.04x10^{-5}	———	———

Table 3.3: Event weights for different mass points of signal events, and for different background processes.

Specific number of events is simulated for both signal events and background processes, so to get the number of expected events at LHC; the different processes are scaled to the correct luminosity (300fb^{-1} at the end of the run-II at $\sqrt{s} = 14$TeV) using the event weight:

$$w = \frac{\sigma \mathcal{L}}{N_{MC}} \tag{3.2}$$

where σ is the cross section of the process, $\mathcal{L}$ is the integrated luminosity which is (300fb^{-1}), and N_{MC} is the number of events generated. Table [3.3] lists event weights for both signal and background.

To identify the signal, we use the "Tight muon ID" [47] as defined in the Delphes card, candidate muons should be isolated so following [45], the isolation variable I is defined in the Delphes configuration file as

$$I = \frac{\sum_{i \neq \mu}^{\Delta R < R,\ p_T(i) > p_T^{min}} p_T(i)}{p_T(\mu)} \tag{3.3}$$

where the denominator is the transverse momentum of the muon. The numerator is the sum of transverse momenta above p_T^{min} (0.1GeV) of all particles that lie within a cone of radius R around the muon, except the muon itself, the cone size is chosen to be R = 0.3, and muons are considered isolated if I <**0.15**.

From the study made at generator level we require that the leading muon p_T must pass the following cut:

1. $\mathrm{p}_T^{leading} > 50$ GeV.

As a first comparison between signal and background, we look at the basic kinematic variables, namely the transverse momentum p_T distribution and pseudorapidity *eta* distribution for the muons, and the leading muon p_T after applying selection 1.

Figure [3.14] shows the $\mathrm{p}_T^{leading}$ of the leading tight muon in the event and p_T of any tight muon in the event distributions. In each figure the solid lines indicate the signal events, one for each mass. The red color indicates the main background processes ($pp \rightarrow$ zz $\rightarrow 4\mu$, $pp \rightarrow$ zz $\rightarrow 4\tau$, $pp \rightarrow$ zz $\rightarrow 2\mu 2\tau$, and $gg \rightarrow$ zz $\rightarrow 4\ell$), the violet color indicates ($t\bar{t}$z), and the green indicates the triple boson processes (WWZ, WZZ, ZZZ). A characteristic property of the signal events is that they always contribute to high values of transverse momentum, and background events tends to be at low values of p_T. Figure [3.15] shows the η and ϕ distributions.

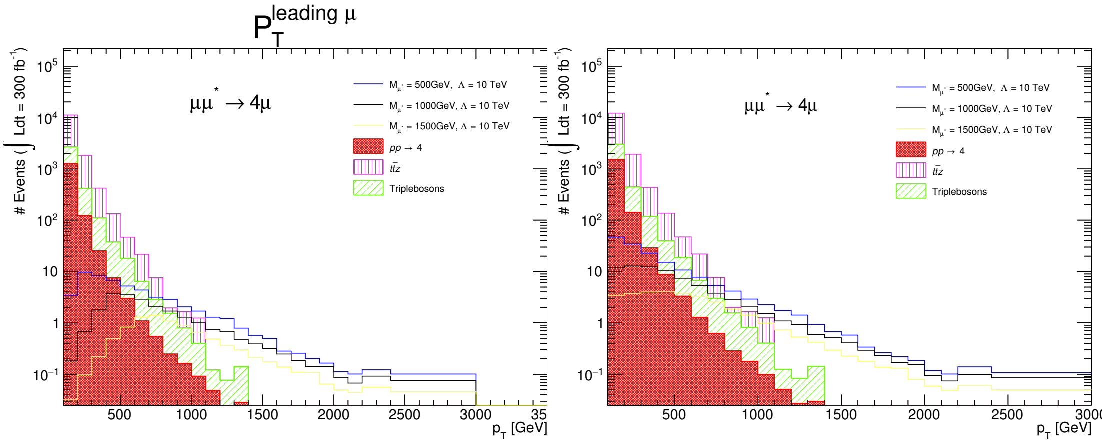

(a) (b)

Figure 3.14: (a) The transverse momentum $p_T^{leading}$ of the leading tight muon in the event (b) The transverse momentum p_T of any tight muon in the event.

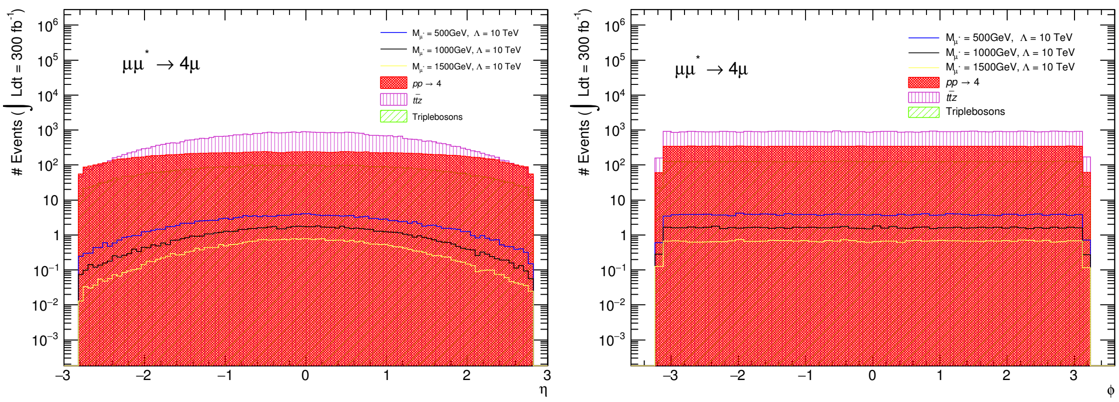

(a) (b)

Figure 3.15: (a) The pesudorapidity η distribution of any tight muon in the event (b) The azimuthal angle ϕ distribution of any tight muon in the event.

Here we come to the next step in extracting the signal from background, that the selection of the Z-boson. Because we want to reconstruct the excited muon mass, we have to reconstruct the mass of the Z-boson first, so:

2. We selec muon pair with opposite charges which is closest to the mass of Z. We apply invariant mass cut 60< $M_{Z1,Z2}$ <120 [GeV]

Figure [3.16] shows the invariant mass of the Z-boson for both signal and background after the invariant mass cut and the transverse momentum of the selected Z-boson.

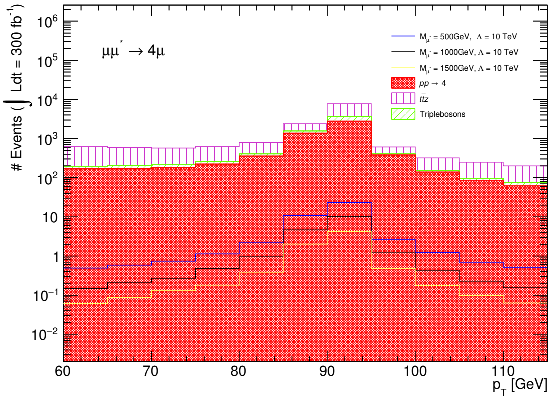

(a)

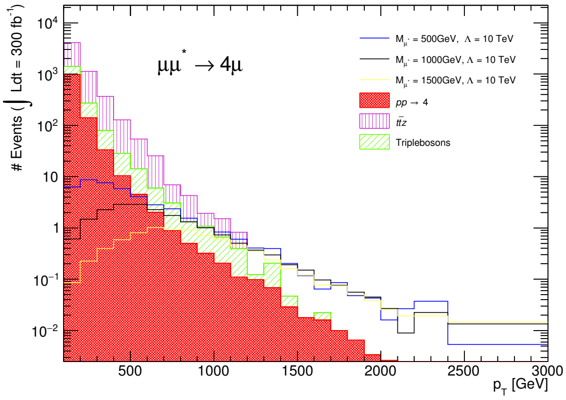

(b)

Figure 3.16: (a) The invariant mass, and (b) the transverse momentum p_T of the selected Z-boson.

The main difference between the signal and the diboson background is the number of Z-bosons. While the signal contains only one Z-boson, the ZZ background should have two. So if the Z-boson is selected from the signal by using two oppositely charged muons, still another possibility of two oppositely charged muons which is Z_{veto}. The mass distribution of the Z_{veto} looks more promising. Signal and background have different shapes.

Most of the background is gathered around the Z-boson mass while most of the signal is in the high mass region. So with the following cut, the background is reduced by a large fraction without losing so much signal events. Although this cut was implemented to discriminate against the diboson production, it is still the dominant background.

3. For the other two muons we apply a Z-veto cut, ($M_{\mu_{CI},\mu_{decay}} >$ 150 GeV), with this cut applied to the muon pairs that are no from the Z we try to reduce the main background pp→ 4μ.

Figure [3.17] the invariant mass of Z_{veto} before and after cut 3.

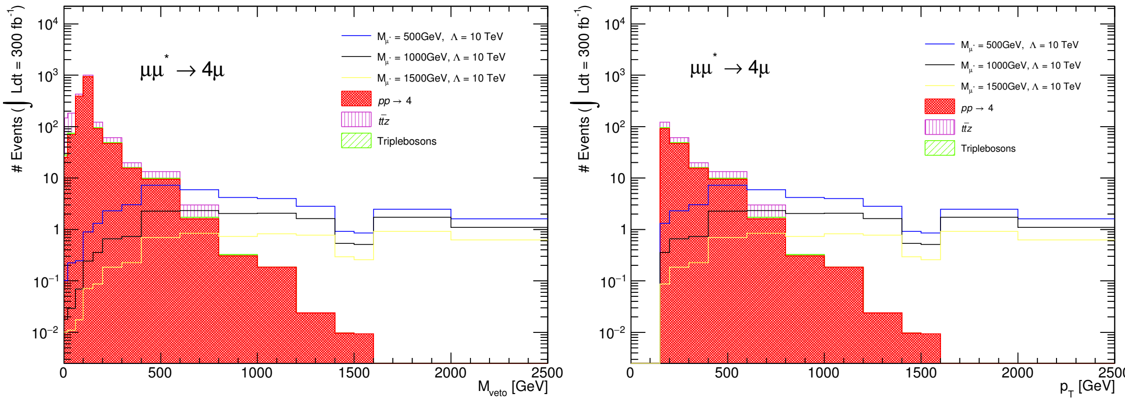

(a) (b)

Figure 3.17: (a) The invariant mass of the other reconstructed muon pair which is Z_{veto} before cut 3, and (b) after cut 3.

For the next selection we will build the minimum invariant mass $M^{3\mu}_{min}$ and the maximum invariant mass $M^{3\mu}_{max}$ which are the most characteristic aspect of the signal and their combination will be used as the most important discriminator for the signal against the background. After reconstructing the Z-boson, one of those distributions should include the reconstructed excited muon. Figure [3.18] illustrates these two distributions.

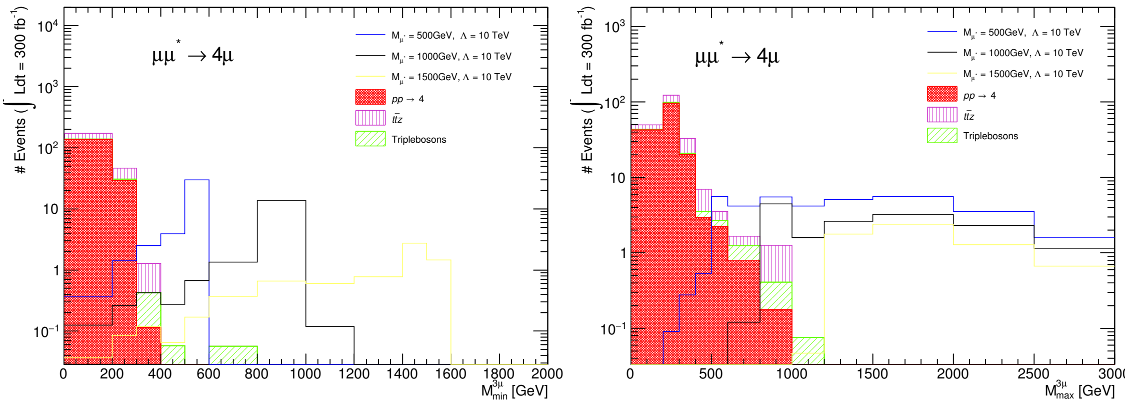

(a) (b)

Figure 3.18: (a) Minimum and (b) Maximum invariant masses in comparison with the background.

We looked at the 4μ system invariant mass and applied the following cut:

4. $M_{4\mu} > 400$, which reduces the background by a large fraction without loosing so much signal events for all mass points.

Figure [3.19] shows the invariant mass of the four muons $M_{4\mu}$ after cut 4.

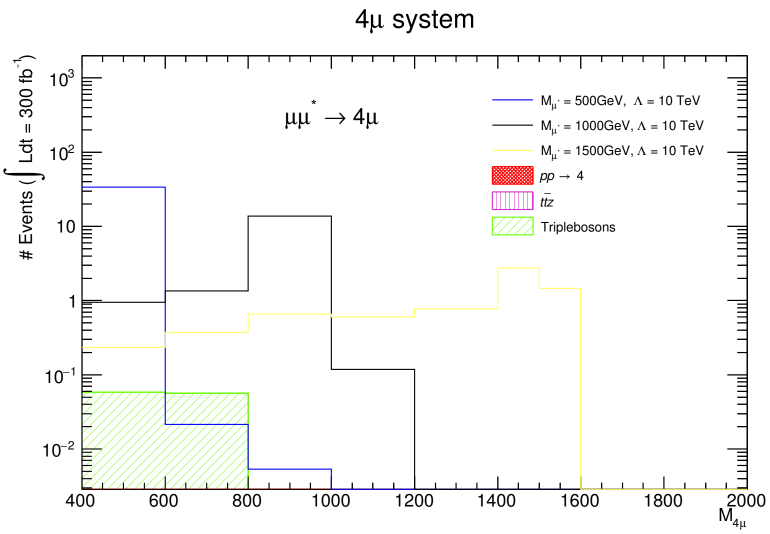

Figure 3.19: The invariant mass of the 4μ system after applying cut 4.

Finally we come to the last step in selecting the signal events, namely the L-shape; we build a 2D plot of $M_{min}^{3\mu}$ and $M_{max}^{3\mu}$ invariant masses, and we get an "inverse L letter" only for signal events. The background in L-shape plot tends to be at low invariant masses, so to discriminate signal against the background we put a mass selection window around the excited muon mass, and this will our final selection which is called "L-shape cut".

The width of these L-shaped depends on the excited muon mass. This width is broader for higher masses of μ^* due to smearing effects of the detector, so the mass window should be broader at higher masses which can easily be done given that high mass regions are practically background free so the mass window is chosen individually for different mass points that by optimizing the signal efficiency. Figure [3.20] shows the effect of L-shape cut for different mass points of excited muons, and for the total background contribution, and figure [3.21] shows the smearing effects of the detector simulation.

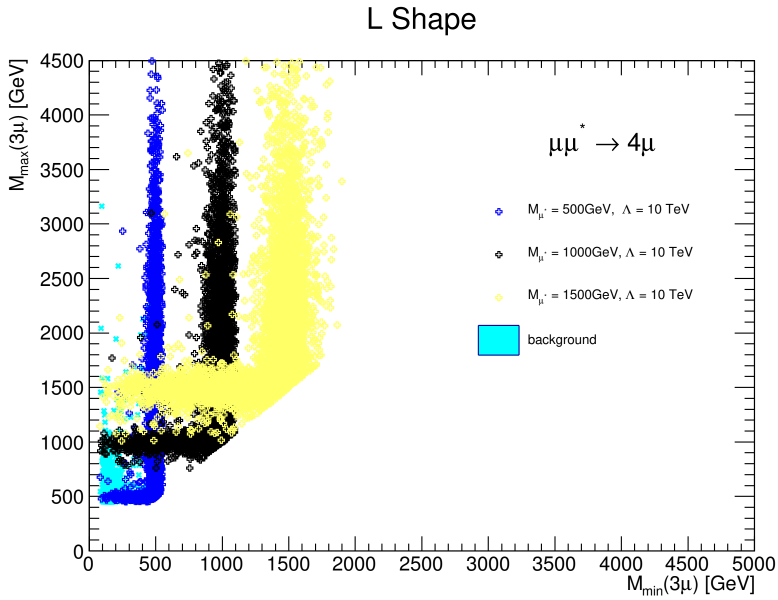

Figure 3.20: L-shape plot for signal and background.

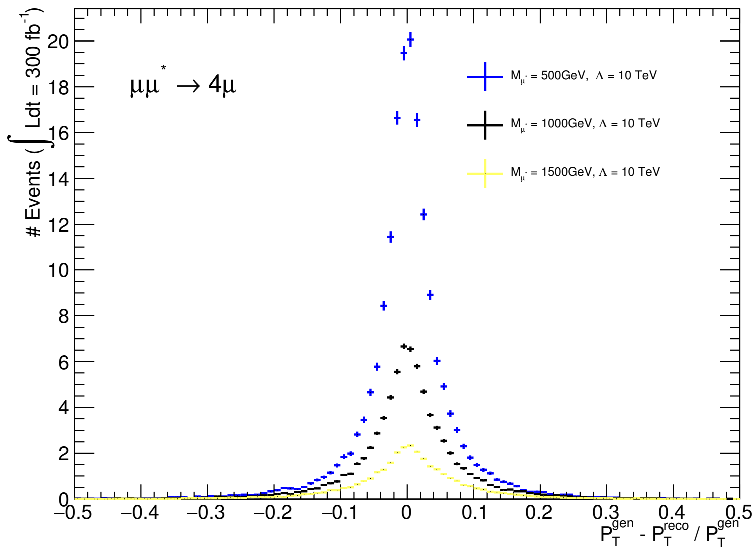

Figure 3.21: The resolution of p_T for different mass points

Detailed number of search mass windows of every mass point of excited muon is given in table [3.4]. For a numerical comparison between signal and background table [3.5] and [3.6] lists event yields of the different mass points of the signal, and the background yield for the given cut flow. The event yield is the number of weighted events.

Mass [GeV]	Lower Boundery [GeV]	Upper Boundery [GeV]
500	450	530
1000	870	1070
1500	1140	1640
2000	1200	2280
2500	1300	2800
3000	1400	3300
3500	1600	3800
4000	1600	4600
4500	1600	5000
5000	1600	6000

Table 3.4: Lower and upper boundaries search mass windows for simulated mass points.

Mass [GeV]	$p_T^{leading}$	Z-veto	$M_{4\mu}$ >150GeV	L-shape
500	53.42	83.04	38.07	37.46
1000	22.41	16.92	16.92	16.76
1500	9.20	7.10	7.1	7.05
2000	3.70	2.90	2.90	2.89
2500	1.45	1.31	1.31	1.12
3000	0.559	0.440	0.440	0.439
3500	0.210	0.167	0.167	0.166
4000	7.82x10^{-2}	6.22x10^{-2}	6.22x10^{-2}	6.21x10^{-2}
4500	2.88x10^{-2}	2.31x10^{-2}	2.31x10^{-2}	2.30x10^{-2}
5000	1.04x10^{-2}	8.31x10^{-3}	8.31x10^{-3}	8.27x10^{-3}

Table 3.5: Summarizing event yields for different mass points of the excited muon for the given cut flow.

Process	$p_T^{leading}$	Z-veto	$M_{4\mu}$ >150GeV	L-shape
$pp \to$ zz $\to 4\mu$	2723	162.0	40.81	4.364
$pp \to$ zz $\to 4\tau$	114	4.34x10^{-3}	0.00	0.00
$pp \to$ zz $\to 2\mu 2\tau$	4090	2.15	5.41x10^{-1}	6.94x10^{-2}
$gg \to$ zz $\to 4\ell$	36.45	1.26	4.97x10^{-1}	5.76x10^{-2}
$pp \to t\bar{t}$z	29178	48.41	22.51	3.82
$pp \to$wwz	3564	3.84	2.37	1.02
$pp \to$wzz	829	1.214	6.43x10^{-1}	2.14x10^{-1}
$pp \to$zzz	217	7.32x10^{-1}	2.23x10^{-1}	4.34x10^{-2}

Table 3.6: Summarizing event yields for the SM background of the given cut flow.

As noted from tables [3.5] and [3.6] that the cut flow used effectively reduce the background by significant fraction without loosing so much signal events.

The efficiency of the cut flow used is plotted in figure [3.22], where the error bars are estimated using the rules of statistical error propagation.

To quantify the discovery potential of excited muon at LHC, the signal significance is computed as follows:

$$SS = \frac{S}{\sqrt{B}} \tag{3.4}$$

where S indicates the number of weighted events of the signal evaluated at each mass point, and B is the number of weighted events of the total background expectations. Figure [3.22] gives a pictorial representation of it.

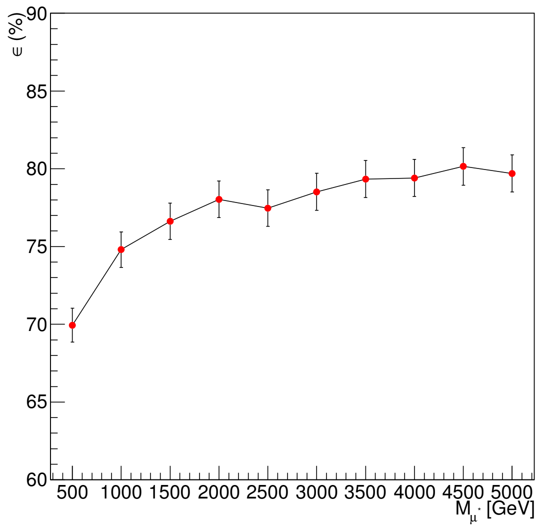

(a)

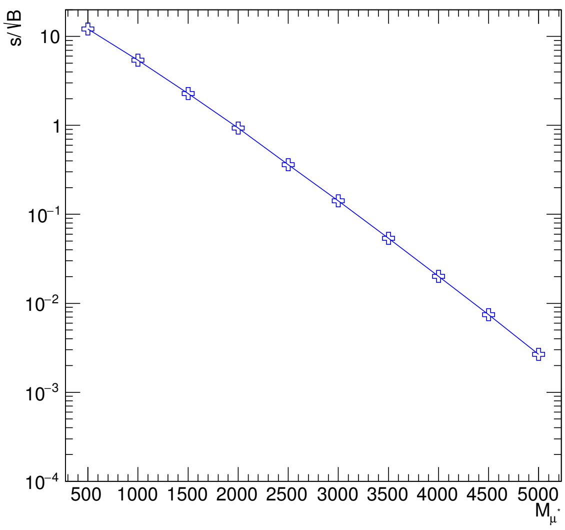

(b)

Figure 3.22: (a) Efficiency of the cut flow and (b) Log Scale of signal significance, as a function of excited muon mass.

As a final comment in this chapter, the event display of Delphes software is used to give a geometrical view of the four muon event at CMS detector. Fig. (3.28) gives 3D view of the CMS detector with the four muon event of the signal, each green line represents one muon. Fig. (3.29) gives cross sectional view of the detector.

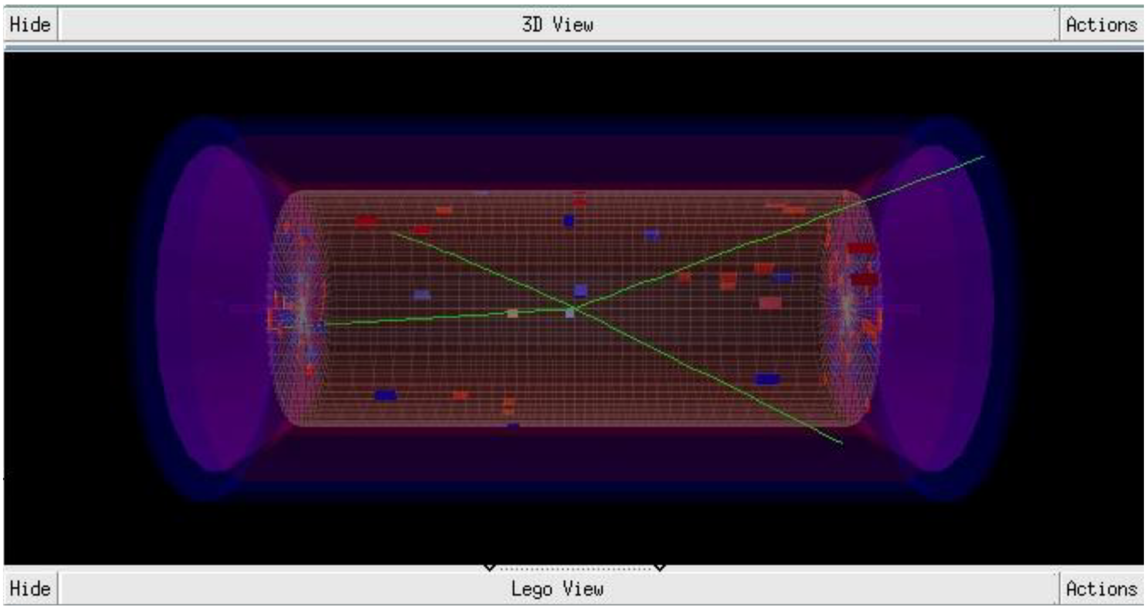

Figure 3.23: 3D view of the CMS detector with the four muon event shown in green.

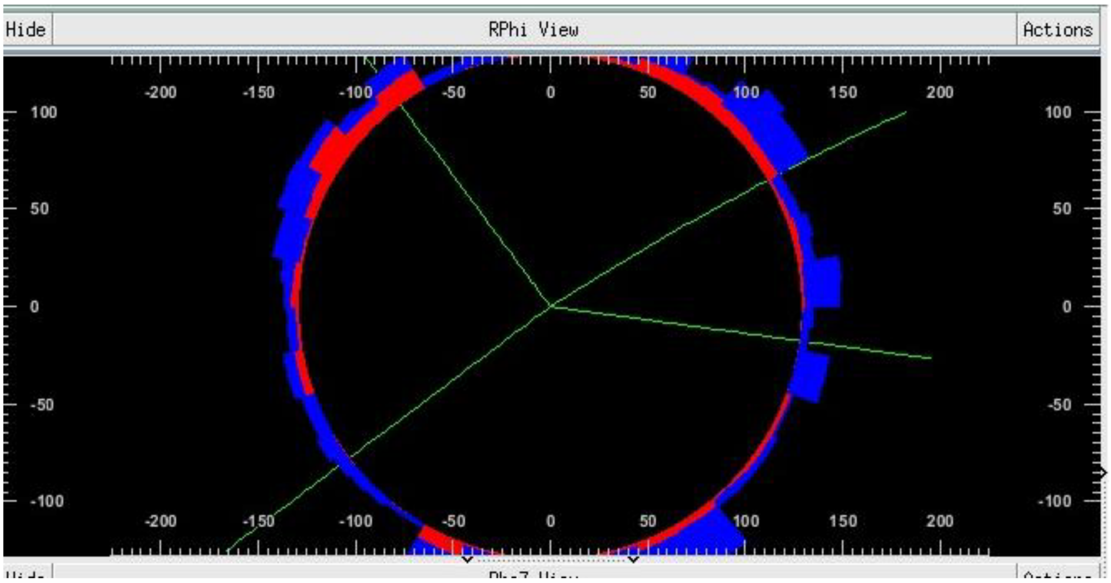

Figure 3.24: Azimuthal angle view of the CMS detector with the four muon event shown in green

Chapter 4

Gas Electron Multiplier Detector

4.1 What is GEM?!

Gas as **E**lectron **M**ultiplier (GEM) technology is being considered for the forward muon upgrade of the CMS experiment in Phase 2 of the CERN - LHC. In this chapter We will state the problems that the actual CMS muon spectrometer will face after the LS1 and LS2 upgrades of the LHC, and motivate the proposition to install GEM detectors in the forward region of CMS instead of RPCs.

GEMs [48, 49, 50] are made out of a 50μm thick Kapton foil coated with a 5μm copper layer on each side, that is chemically drilled to create a honeycomb pattern of holes, as represented in figure [4.1].The holes have a diameter of 70μm on both ends and a diameter of 50μm in the middle. They are separated by 140μm.

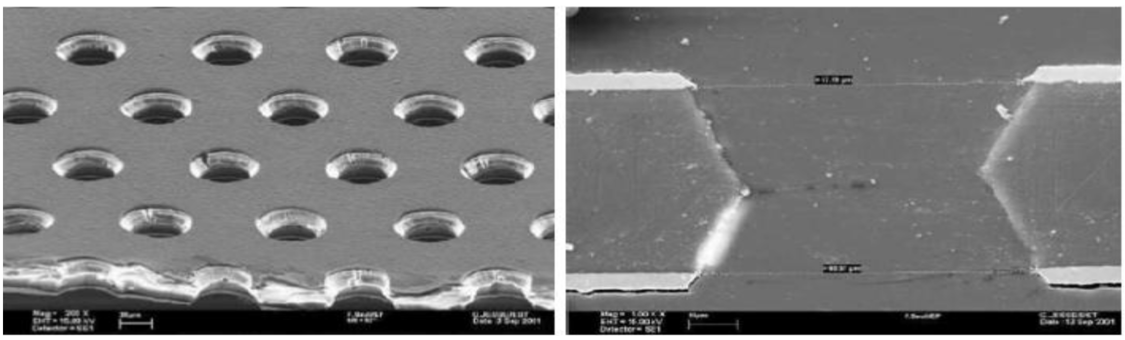

Figure 4.1: Electron microscope view of the honeycomb pattern of holes in a GEM foil [51].

Three GEM foils are stretched and spaced by a few millimeters using a frame to form a *Triple-GEM detector*. A cathode plane is placed on one side and a series of anode strips for the readout on the other.

Figure [4.2] illustrates the layers that compose a chamber. GEM detectors have the same trapezoidal shape as CSCs as they would be installed in the end-caps.

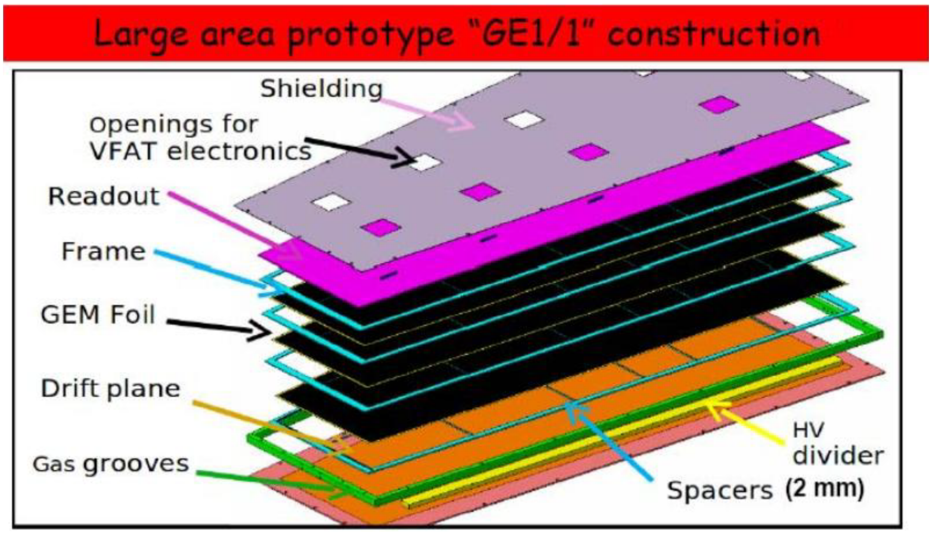

Figure 4.2: Mechanical construction of the large-area chamber.

The detector is filled with a suitable gas mixture, and a voltage difference is applied between the two copper layers of each GEM foil to create a strong electric field inside the holes that act as multipliers. The field directs the electrons towards the regions where they will be accelerated and create avalanches, so even a small voltage difference generates the intense fields required to initiate avalanches. This process is show in figure [4.3].

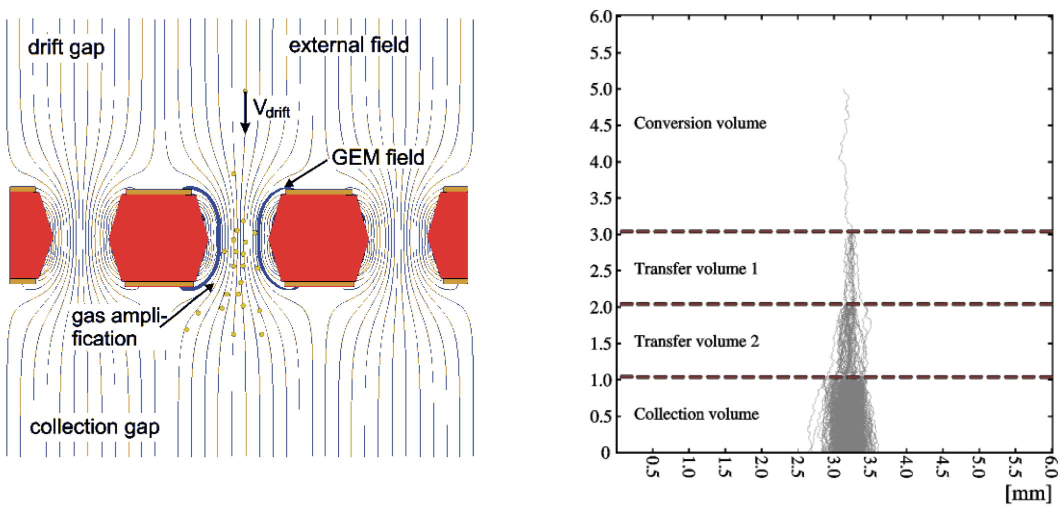

Figure 4.3: (left) Representation of the electric field created inside the holes, (Right) Signal amplification for a Triple-GEM detector.

4.2 CMS Muon System Upgrade

The standard RPCs are not designed to operate at the high rates of particles that will be reached after LS2 and will lose efficiency. GEM detectors already used in other experiments present the opportunity to equip the vacant region with detectors that have proven to maintain a spatial resolution of the order of 100μm, a time resolution below 5ns, and a detection efficiency above 98% even at elevated fluxes. So GEM first implementation in CMS experiment is planned for the GE1/1 station in the 1.55< η <2.18 region of the muon endcap mainly to control muon level-1 trigger rates after the second long LHC shutdown [52].

Figure [4.4] shows the quadrant of the muon system, where installation of GE1/1 detectors is proposed [52]. This installation will help to restore redundancy for tracking and triggering in the muon system, as GEM detectors provide very precise tracking information due to high spatial resolution. Lack of redundancy in this region will become critical during the HL-LHC phase after LS2.

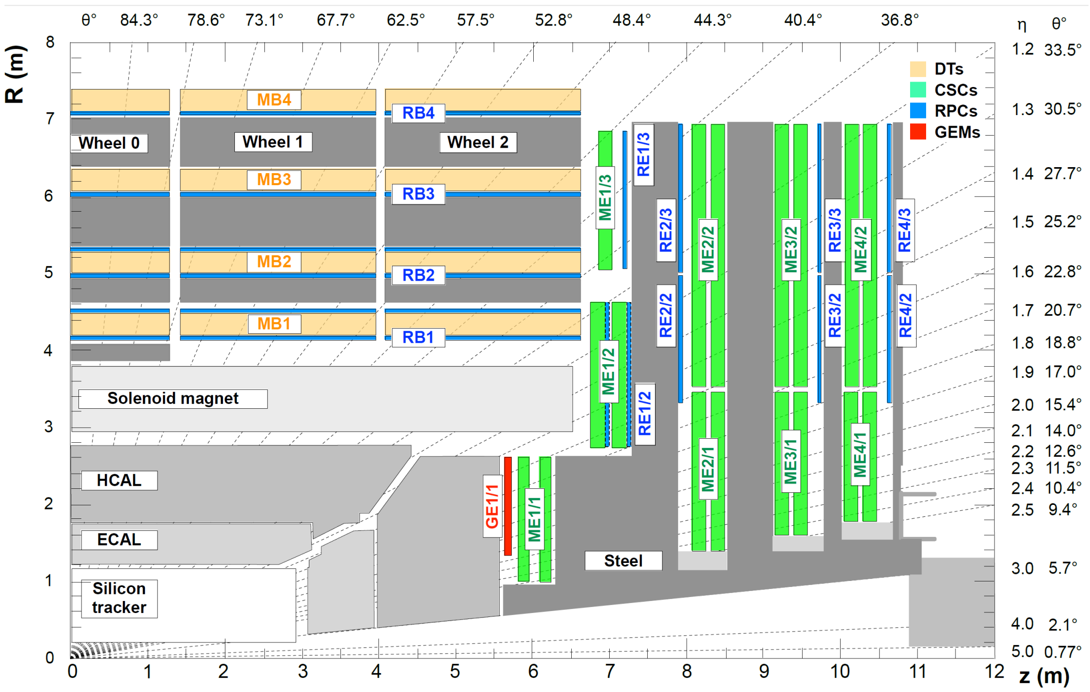

Figure 4.4: A quadrant of the R−z cross-section of the CMS detector, highlighting in red the location of the proposed GE1/1 detector within the CMS muon system.

In the GE1/1 muon system, a pair of *Triple-GEM chambers* is combined to form a *superchamber*. Each superchamber covers a $\sim 10^o$ sector, so that 72 superchambers are required (36 in each endcap) to form a ring of superchambers that gives full azimuthal coverage. The superchambers alternate in ϕ between long ($1.55< \eta <2.18$) and short ($1.61< \eta <2.18$) versions, as dictated by the mechanical envelope of the existing endcap. Each endcap holds 18 long and 18 short superchambers. Figure [4.5] shows the superchamber and one endcap GEM installation.

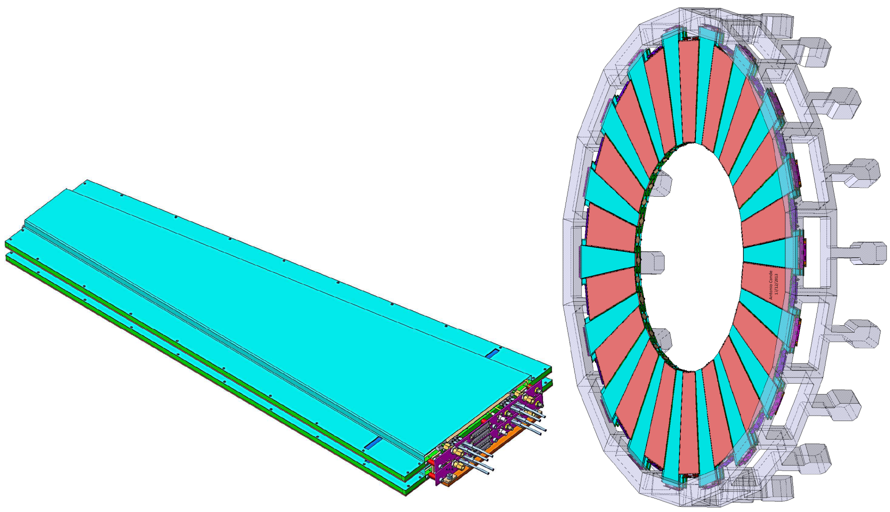

Figure 4.5: (Left) A pair of GEM chambers form a superchamber. (Right) Long and short chambers are combined to maximize the instrumentation within given mechanical constraints in the endcap.

To increase redundancy, and make use of the free space, the installation of GEM detectors has been proposed by the CMS GEM Collaboration. Even though GEMs are proposed to be installed during LS2, the CMS GEM Collaboration has been allowed to install four prototypes in CMS during March 2014, at the end of LS1, in order to test the mechanical feasibility of the installation.

Because of the high penetrating power of muons, their momenta can also be affected through their motion in solid-iron return yoke of the magnet in CMS detector. For this kind of interaction, however, the influence of multiple scattering (known as Coulomb scattering) cannot be neglected.

Through their motion in the iron segment of thickness L, muons will obtain transverse momentum ΔP_T due to multiple scattering as shown in figure [4.6].

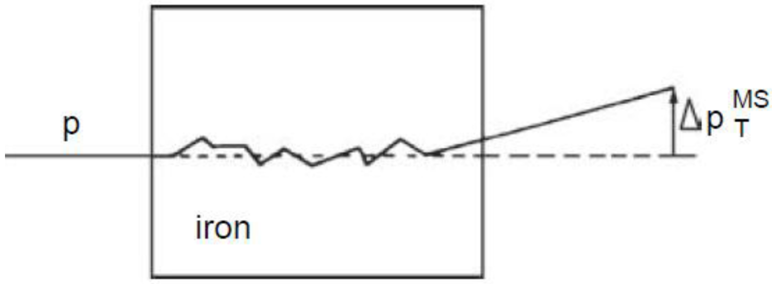

Figure 4.6: Illustration of the multiple-scattering error.

In addition to the track measuring error in CMS tracker system one has to consider the multiple-scattering error. For the general case of nonrelativistic velocities β, the momentum resolution is given by:

$$\frac{\sigma(p_T)}{p_T}|^{MS} = 0.045\frac{1}{\beta}\frac{1}{B[T]\sqrt{L[m]X_o[m]}}$$

Where X_o is the average radiation length of the material traversed by the muon, and B is the magnetic field strength.

Cathode Strips chambers alone misidentify multiply scattered lower p_T muons as high PT muons. This problem can be overcome by introducing GEM detectors in conjunction with the CSC system as shown in figure [4.7], together they provide an accurate measurement of the muon bending angle that is not affected by multiple scattering. This discriminates lower p_T muons from higher p_T muons and reduces the soft muon rate at the level-1 trigger as shown in figure [4.8], which will help control the muon trigger rate at the high luminosity LHC.

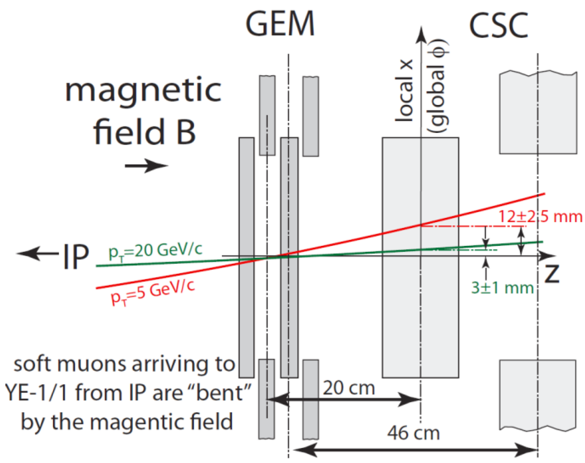

Figure 4.7: GEM and CSC system in each station enlarge the lever arm for a bending angle measurement unaffected by multiple scattering.

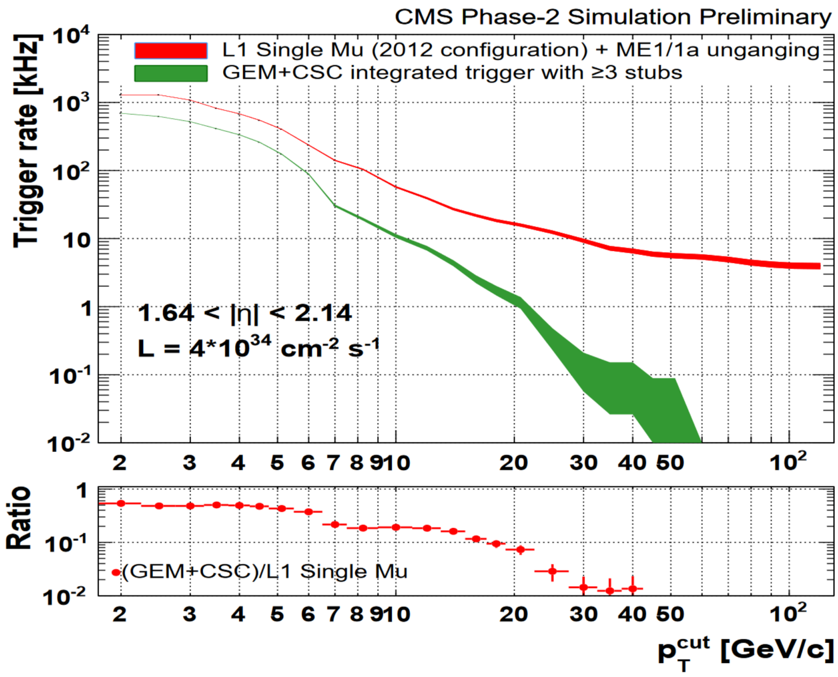

Figure 4.8: Simulation of the inclusive muon trigger rate expected for the LHC Phase 2 as function of the Level-1 p_T trigger threshold.

4.3 Performance study

As explained in the last chapter; that the muons of excited muon production and decay is characterized by hard p_T specturm which presents the opportunity to study the performance of the muon system of CMS especially at high values of η. So physics signal events of excited muons to four muons pp$\rightarrow$ $\mu\mu^* \rightarrow \mu$Z$\rightarrow$ 4μ, are generated using PYTHIA8 within the framework of CMS Software (CMSSW) at $\sqrt{s}$ = 14 TeV, Λ=10TeV, and M_{μ^*}=0.5TeV, then they are fed into detector simulation tool GEANT4 for detector geometry 2023 which contains GEM detector installed.

Figure [4.9] and figure [4.10] shows the occupancy plots for the two layers of GEM chambers installed at both endcaps, as can be seen the installation of GEM introduces redundancy in tracking and reconstruction capabilities for the most challenging region for muon detection, i.e. at high η.

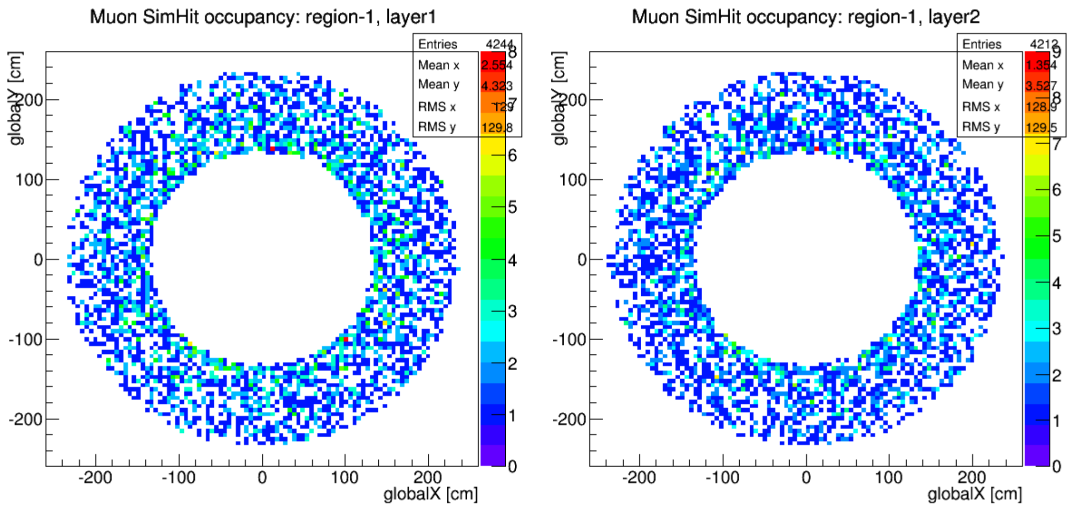

(a) (b)

Figure 4.9: (a) Simulated Hits (*SimHits*) of muons in GE1/1 layer1, and (b) layer2 at one end-cap.

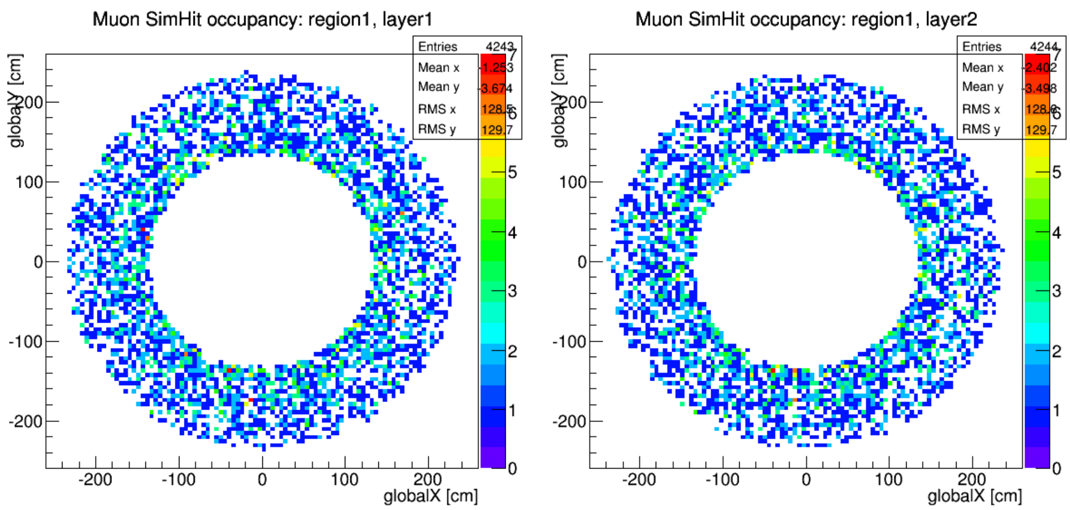

(a) (b)

Figure 4.10: (a) Simulated Hits (*SimHits*) of muons in GE1/1 layer1, and (b) layer2 at the other end-cap.

At high η the muon track projections in the bending plane are also the shortest giving rise to worsening momentum resolution compared with the central region. In figure [4.11] we can see the momentum resolution of muons using the reconstructed inner track (reconstructed in the tracker) and global track (reconstructed in both the tracker and the muon system) by requiring the number of matches of RPC chambers greater than zero which is shown in red, and the number of matches of GEM chambers are greater than zero as well which is shown in blue. As can be seen adding GEM chambers results in an improved momentum resolution.

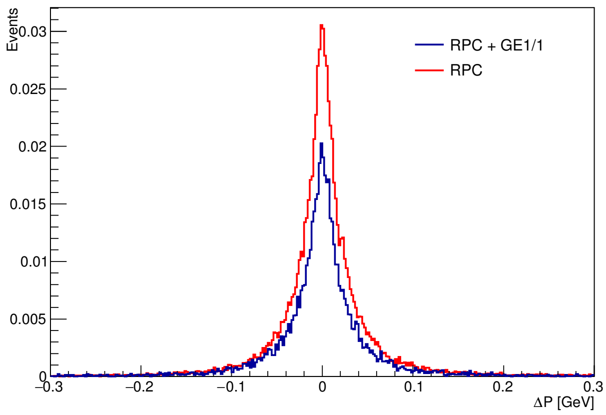

Figure 4.11: Momentum resolution between tracks with a GE1/1 added to the present muon system.

Furthermore the effect of high spatial resolution of GEM is illustrated in figure [4.12] where the resolution between simulated hits and reconstructed hits is shown, and a nearly diagonal behaviour is noticed.

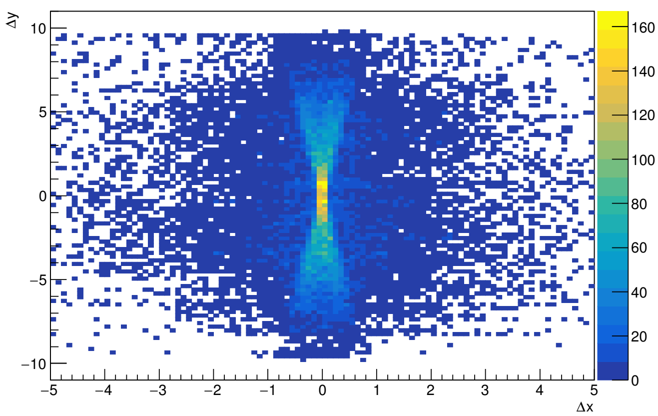

Figure 4.12: Resoultion between *SimHits* and *RecHits* in 2D.

Each SimHit knows the ID of the detector it was produced in, position, direction, **T**ime **O**f **F**light (TOF) when it was produced after the beam interaction, and the energy loss in this hit. Figure [4.13] shows the TOF, where it can be seen that is around 20ns smaller than the Bunch Crossing (25ns) which is beneficial at the operation of phase II of LHC.

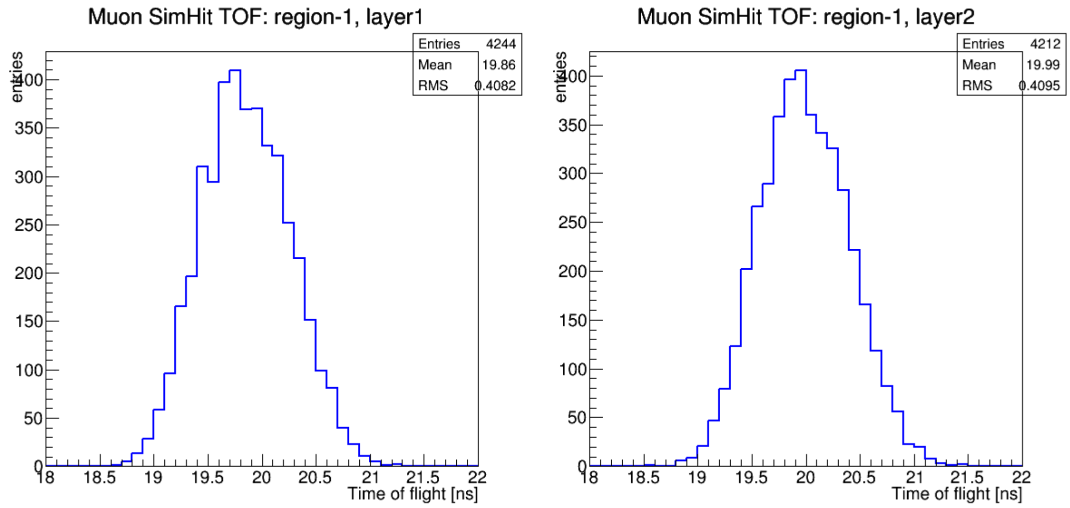

(a) (b)

Figure 4.13: (a) Time of flight of muons in layer1, and (b) layer2 at one end-cap.

The track properties of muons in GEM detector are shown in figure [4.14], as it can be shown there is a plateau in the pseudo-rapidity η and also in ϕ distribution.

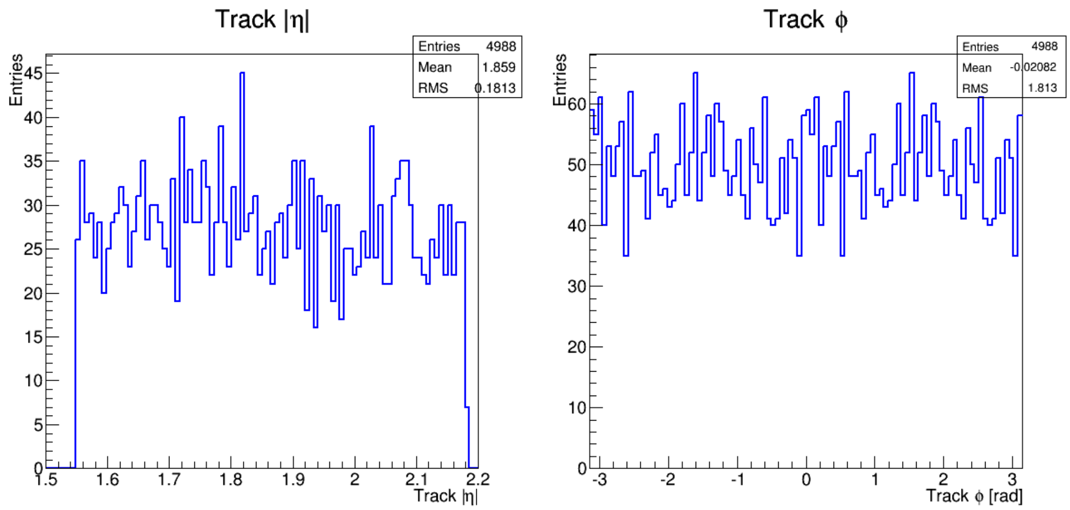

(a) (b)

Figure 4.14: (a) Muons track in GEM detector as function in η, and (b) Muons track in GEM detector as function in ϕ.

Figure [4.15] shows the reconstruction efficiency of GEM as a function of ϕ, as it be shown from efficiency plots, that the detection efficiency approaches 99% in the currently dead region 1.5< η <2.2.

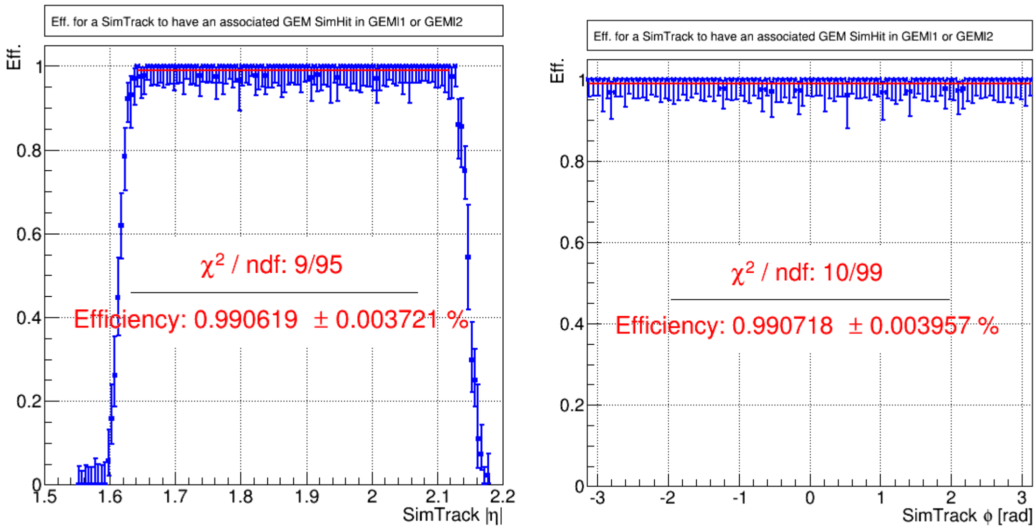

(a) (b)

Figure 4.15: (a) Efficiency of GEM detector in the region of interest 1.5< η <2.2, and (b) Efficiency of GEM detector as function of ϕ.

Adding the GEM subsystem improves momentum resolution for high-p$_T$ endcap muons in the TeV region and increases the robustness of the muon trigger by providing an independent second trigger path for the forward muon region. These attributes of the proposed GEM system will strengthen the ability of CMS to control its muon trigger rates in the ever more challenging running environments of the future. Most weaknesses present in the ME1/1 system will be mitigated thereby affording fully efficient and clean reconstruction of muons by improving muon momentum resolution and providing a highly efficient trigger and reconstruction capability reached using the complementary, robustness and redundancy of two independent technologies [53].

Chapter 5

Conclusion

Although the Standard Model of Particle Physic is very successful, but the plethora of particles, large number of free parameters, and the three generations of matter particles, motivate the search of a complete theory. Compositeness models are motivated by the fore-mentioned shortcomings of the SM, excited states within the framework of compositeness models have a unique signature in CMS detector.

To summarize the work done in this thesis, we have investigated the discovery potential of excited muons μ^* at center of mass energy $\sqrt{s} = 14$ TeV and integrated luminosity of 300fb^{-1} using four muons final state. In any model of lepton compositeness, excited states occur naturally and these couples to the SM counterparts through a corresponding term in an effective Lagrangian. The considered channel is the decay channel pp$\rightarrow \mu\mu \rightarrow \mu\mu$Z, with the Z gauge boson decaying into two muons.

The presence of excited muon would alter the shape of kinematical variables which would be visible at interaction scale in the TeV region. The extent of these changes depends on the mass of the excited muon M_{μ^*} and the compositeness scale Λ.

After applying selection criteria to enhance the signal significance, comparison between signal events and SM background shows that have unique features, and so defines discriminating variables that can be used to enhance signal against background.

The invariant mass distribution of the three muons forming the excited muon shows a bump in what is called maximum and minimum invariant mass plots, upon forming a 2D plot of maximum-minimum invariant mass plots, a potential signal will form an inverse L-shape around its assumed mass, the width of the mass window of excited muon increase with increasing its mass due to increasing mass resolution of muons.

In conclusion we believe that if muons have substructure, the excited state should be observed in 4μ final state at the CMS detector with 300fb^{-1} of data. If such signals are indeed found in the next run of LHC, in later years the excess of the SM expectations could further stamp for their existence.

GEM detectors are proposed in the run-II of LHC in CMS experiment, performance study of GEM detectors using four muon final state shows a 98% efficiency in the desired η range $1.55< \eta <2.18$, which allows GEMs to be used for triggering tasks. The design of GEMs allows them to be used in the region of high interaction rates.

Bibliography

[1] C. Quigg. *Gauge Theories of the Strong, Weak, and Electromagnetic Interactions.* Addison-Wesley, 1983.

[2] G.L. Kane. *Modern Elementray Particle Physics.* Addison-Wesley, 1993.

[3] P.A.M. Dirac. “The Quantum Theory of Emission and Absorption of Radiation”. In: *Proc. Royal Society A* 114 (1927), p. 243.

[4] V. Fock. “Local Gauge Invariance in QED”. In: *Zeitschrift für Physik* 39 (1927), p. 226.

[5] H. Weyl. “Local Gauge Invariance in QED”. In: *Zeitschrift für Physik* 56 (1929), p. 230.

[6] D. Griffiths. *Introduction to Elementary Particle Physics.* WILEY-VCH, 2009, pp. 307–346.

[7] M. Thomason. *Modern Particle Physics.* Cambridge University Press, 2013, pp. 242–284.

[8] P.W. Higgs. “Broken Symmetries, mass-less particles, and gauge fields”. In: *Phys. Lett.* 12 (1964), pp. 132–133.

[9] M. Kamionkowski. “Dark Matter and Dark Energy”. In: *arXiv:0706.2986 [astro-ph]* (2007).

[10] et al. Alvarez-Gaum. “Review of Particle Physics”. In: *Phys. Lett. B* 667 (2008), pp. 31–92.

[11] J.C. Pati and A. Salam. “Lepton Number as the Fourth Color”. In: *Phys. Rev. D* 10 (1974), p. 275.

[12] J.C. Pati and A. Salam. “Lepton Number as the Fourth Color”. In: *Phys. Rev. D* 11 (1975), p. 703.

[13] K.D. Lane. E.J. Eichten and M E. Peskin. “New Tests for Quark and Lepton Substructure”. In: *Phys. Rev. Lett.* 83 (1983), p. 811.

[14] M. Spira U. Baur and P.M. Zerwas. “Excited-quark and Lepton-Production at Hadron Colliders”. In: *Phys. Rev. D* D42 (1990), p. 815.

[15] S.M. Lietti O.J.P. Eboli and P. Mathews. “Excited Leptons at the CERN Large Hadron Collider”. In: *Phys. Rev. D* 65 (2002).

[16] The ZEUS Collaboration. “A search for excited fermions in e+ p collisions at HERA”. In: *Zeitschrift für Physik C Particles and Fields* 76 (1997), pp. 631–646.

[17] B. Tome. “Search for Excited Fermions”. In: *Proceedings of Science* 313 (HEP-2005).

[18] H1 Collaboration. “A search for excited fermions at HERA”. In: *DESY-Deutsches Elektronen-Synchrotron* -00-102 (2000).

[19] OPAL Collaboration. “Search for Charged Excited Leptons in e+ e- Collisions at $\sqrt{s}$ =183- 209 GeV”. In: *Phys. Lett. B* 544 (2002), pp. 57–72.

[20] CDF Collaboration. “Search for excited and exotic electrons in the egamma decay channel in pp collisions at $\sqrt{s} = 1.96$ TeV”. In: *Phys. Rev. Lett.* 94 (2005).

[21] D0 Collaboration. “Search for Excited Electrons in p-p collisions at $\sqrt{s} = 1.96$ TeV”. In: *Phys. Rev. D* 77 (2008).

[22] CMS Collabration. “Search for excited leptons in p-p collisions at $\sqrt{s} = 7$ TeV”. In: *Phys. Lett. B* 704 (2011), pp. 143–162.

[23] ATLAS Collabration. “Search for excited electrons and muons in $\sqrt{s} = 8$ TeV proton–proton collisions with the ATLAS detector”. In: *New J. Phys.* 15 (2013).

[24] L. Evans and P. Byrant. “CERN Large Hadron Collider: Accelerator and Experiments: LHC Machine”. In: *J. Instrum.* 3 (2008).

[25] ATLAS Collaboration. *ATLAS: technical proposal for a general-purpose pp experiment at the Large Hadron Collider at CERN.* Vol. 22. CERN/LHCC, 1994.

[26] CMS Collaboration. *The Compact Muon Solenoid Technical Proposal.* Vol. 22. CERN/LHCC, 1994.

[27] ALICE Collaboration. *ALICE: Technical proposal for a Large Ion collider Experiment at the CERN LHC.* Vol. 22. CERN/LHCC, 1995.

[28] LHCb Collaboration. *LHCb: Technical Proposal.* Vol. 22. CERN/LHCC, 1998.

[29] LHC Commissioning. *Longer term LHC schedule.* `https://lhc-commissioning.web.cern.ch/lhc-commissioning/schedule/LHC-long-term.htm`.

[30] CMS Collaboration. “The CMS experiment at the CERN LHC. The Compact Muon Solenoid experiment”. In: *J. Instrum.* 3 (2008).

[31] CMS Collaboration. “The Tracker Project, Technical Design Report”. In: *CERN/LHCC* 6 (1998).

[32] CMS Collaboration. “The Electromagnetic Calorimeter Project, Technical Design-Report”. In: *CERN/LHCC* 33 (1997).

[33] CMS Collaboration. “The Hadron Calorimeter Project, Technical Design Report”. In: *CERN/LHCC* 31 (1997).

[34] CMS Collaboration. “The Magnet Project, Technical Design Report”. In: *CERN/LHCC* 10 (1997).

[35] CMS Collaboration. “Precise Mapping of the Magnetic Field in the CMS Barrel Yoke using Cosmic Rays”. In: *J. Instrum.* 10 (2010).

[36] et. al J. Beringer. “Review of Particle Physics”. In: *Phys. Rev. D* 86 (2012).

[37] CMS Collaboration. *Muon Drift Tubes.* URL: `http://cms.web.cern.ch/news/muon-drift-tubes`.

[38] CMS Collaboration. *Cathode Strip Chambers.* URL: `http://cms.web.cern.ch/news/cathode-strip-chambers`.

[39] F. Thyssen. “Performance of the Resistive Plate Chambers in the CMS experiment”. In: *J. Instrum.* 7 (2012).

[40] CMS Collaboration. “CMS: The Trigger and Data Acquisition Project: The Level-1 Trigger Technical Design Report”. In: *CERN/LHCC* Volume-I (2000).

[41] CMS Collaboration. “CMS: The Trigger and Data Acquisition Project: Data Acquisition and High-Level Trigger Technical Design Report”. In: *CERN/LHCC* Volume-II (2002).

[42] S. Mrenna T. Sjostrand and P.Z. Skands. “PYTHIA 6.4 physics and manual”. In: *JHEP* 05 (2006).

[43] J. Alwall et al. “Madgraph5 Going Beyond”. In: *JHEP* 128 (2011).

[44] G. Corcella et al. “HERWIG 6: An Event generator for hadron emission reactions with interfering gluons (including supersymmetric processes)”. In: *JHEP* 010 (2001).

[45] J. de Favereau et al. “DELPHES 3, A modular framework for fast simulation of a generic collider experiment”. In: *JHEP* 057 (2014).

[46] CMS Collobartion. “Measurement of the properties of a Higgs boson in the four-lepton final state”. In: *Phys. Rev. D* 89 (2014).

[47] CMS Collobration Muon POG. *Tight Muon ID*. URL: `https://twiki.cern.ch/twiki/bin/viewauth/CMS/SWGuideMuonIdRun2#Tigh%20_Muon`.

[48] A. Ball A. Sharma. “CMS Technical Design Report for the Muon Endcap GEM Upgrade”. In: *CERN-LHCC* 012 (2015).

[49] et al. C. Altunbas. “Construction, test and commissioning of the triple-gem tracking detector for compass”. In: *Nuclear Instruments and Methods in Physics Research A.* 90 (2002), pp. 177–203.

[50] et. al. M. Tytgat. “Construction and Performance of Large-Area Triple-GEM Prototypes for Future Upgrades of the CMS Forward Muon System.” In: *Conference: C11-10-23.1* (2011), pp. 1019–1025.

[51] P. E. Karchin. “Performance of a Large-Area Triple-GEM Detector in a Particle Beam.” In: *Physics Procedia* 37 (2012), pp. 561–566.

[52] et. al. D. Abbaneo. “Performance of a Large-Area GEM Detector Prototype for the Upgrade of the CMS Muon Endcap System”. In: *Conference: C14-11-08* (2014), p.7431249.

[53] et. al. D. Abbaneo. “A GEM Detector System for an Upgrade of the High-eta Muon Endcap Stations GE1/1 + ME1/1 in CMS”. In: *arXiv:1211.1494 [physics.ins-det]* (2012).